JPL Publication 12-16

HyspIRI Thermal Infrared (TIR) Band Study Report

Michael S. Ramsey
University of Pittsburgh
Pittsburgh, PA

Vincent J. Realmuto
Glynn C. Hulley
Simon J. Hook
Jet Propulsion Laboratory
Pasadena, CA

National Aeronautics and Space Administration

Jet Propulsion Laboratory
California Institute of Technology
Pasadena, California

Oct 2012

This research was carried out at the Jet Propulsion Laboratory, California Institute of Technology, and at the University of Pittsburgh under a contract with the National Aeronautics and Space Administration.

Revisions:

Version 1.0 draft by Glynn Hulley, 10/23/2012
Section 5 updated by Vince Realmuto, 10/25/2012
Minor edits and formatting by Peter Basch (JPL editor), 10/26/2012
Edits in all sections by Mike Ramsey, 11/1/2012

Notes:

Section 5 research was conducted by Realmuto at the Jet Propulsion Laboratory, California Institute of Technology.
Section 6 research was conducted by P.I. Ramsey at the University of Pittsburgh, PA.
Section 7.2 research and development of MAGI was conducted by Ramsey, P.I. Hall and the MAGI team at Aerospace Corporation, El Segundo, CA.
Section 7.1 development and research of HyTES was conducted by P.I. Hook and the HyTES team at the Jet Propulsion Laboratory, California Institute of Technology.

Contacts

Readers seeking additional information about this study may contact the following researchers:

Vincent J. Realmuto
MS 183-501
Jet Propulsion Laboratory
4800 Oak Grove Dr.
Pasadena, CA 91109
Email: vincent.j.realmuto@jpl.nasa.gov
Office: (818) 354-1824

Michael S. Ramsey
Department of Geology & Planetary Science
University of Pittsburgh
4107 O'Hara Street, room 200
Pittsburgh, PA 15260
Phone: (412) 624-8772; Fax: (412) 624-3914
Email: mramsey@pitt.edu

Glynn C. Hulley
MS 183-501
Jet Propulsion Laboratory
4800 Oak Grove Dr.
Pasadena, CA 91109
Email: glynn.hulley@jpl.nasa.gov
Office: (818) 354-2979

Simon J. Hook
MS 183-501
Jet Propulsion Laboratory
4800 Oak Grove Dr.
Pasadena, CA 91109
Email: simon.j.hook@jpl.nasa.gov
Office: (818) 354-0974

Abstract

One of the many science questions that will be addressed by the Hyperspectral Infrared Imager (HyspIRI) mission will be to help identify natural hazards such as volcanic eruptions and any associated precursor activity, and it will also map the mineralogical composition of the natural and urban land surface. To answer these questions, the HyspIRI satellite includes a thermal infrared (TIR) multispectral scanner with seven spectral bands in the thermal infrared (TIR) between 7 and 12 μm and one band in the mid-infrared between 3 and 5 μm designed to measure hot targets. The TIR bands have a NEΔT of <0.2 K at 300 K and all bands have a spatial scale of 60 m. A critical aspect of HyspIRI being successful at answering the science questions associated with the HyspIRI science tractability matrix is placement of the 7 TIR bands in the 7–12 μm spectral region. In order to help determine the optimum positions for the TIR bands, a small team was assembled to conduct a study report based on laboratory, spaceborne, and airborne data.

Contents

Figures

Tables

1 Introduction

The Hyperspectral Infrared Imager (HyspIRI) mission will provide an unprecedented capability to assess how ecosystems respond to natural and human-induced changes. It will help us assess the status of biodiversity around the world and the role of different biological communities on land and within inland water bodies, as well as coastal zones and, at reduced resolution, in the ocean [*HyspIRI*, 2008]. Furthermore, it will help identify natural hazards—in particular, volcanic eruptions and any associated precursor activity—and it will map the mineralogical composition of the natural and urban land surface. The mission will advance our scientific understanding of how the Earth is changing as well as provide valuable societal benefit in understanding and tracking dynamic events such as volcanoes and wildfires.

HyspIRI includes two instruments: a visible shortwave infrared (VSWIR) imaging spectrometer operating between 380 and 2500 nm in 10-nm contiguous bands and a thermal infrared (TIR) multispectral scanner with eight spectral bands operating between 4 and 12 μm. Both instruments acquire data with a spatial resolution of 60 m from the nominal orbit altitude. The VSWIR and TIR instruments have revisit times of 19 and 5 days with swath widths of 145 and 600 km, respectively.

In terms of spectral and spatial resolution, the HyspIRI TIR measurement derives its heritage from the Advanced Spaceborne Thermal Emission and Reflection radiometer (ASTER) instrument, a five-channel multispectral TIR scanner that was launched on NASA's Terra spacecraft in December 1999 with a 90-m spatial resolution and revisit time of 16 days [*Yamaguchi et al.*, 1998]. The ASTER band positions in turn were derived from the NASA airborne Thermal Infrared Multispectral Scanner (TIMS), a precursor airborne instrument used in preparation for ASTER that had six TIR bands. One of the most important aspects of a TIR instrument's design is determining optimal number, positions, and detection thresholds of the TIR channels. Positions of the bands within the TIR region will influence the ability to better quantitatively map: 1) SO_2 from volcanic and anthropogenic sources, 2) minerals on the Earth's surface such as feldspars, carbonates, and silicates, as well as 3) urban materials.

The remainder of the document will detail case studies involving volcanic emissions and surface mineral mapping to optimize the HyspIRI TIR band positions in order to answer the

relevant Earth Science questions. The data used in this study include satellite, laboratory, and airborne data.

2 HyspIRI instrument characteristics

The TIR instrument will acquire data in eight spectral bands, seven of which are located in the thermal infrared part of the electromagnetic spectrum between 7 and 13 µm shown in Figure 1; the remaining band is located in the mid-infrared part of the spectrum around 4 µm. The center position and width of each band is provided in Table 1. The exact spectral location of each band has not been determined; the nominal locations provided here are based on the measurement requirements identified in the science-traceability matrices, which included recognition that related data was acquired by other sensors such as ASTER and the Moderate Resolution Imaging Spectroradiometer (MODIS). HyspIRI will contribute to maintaining a longtime series of these measurements. For example, the positions of three of the TIR bands closely match the first three thermal bands of ASTER, while two of the TIR bands match bands of ASTER and MODIS typically used for split-window type applications (ASTER bands 12–14 and MODIS bands 28, 31, 32). It is expected that small adjustments to the band positions will be made based on ongoing science activities.

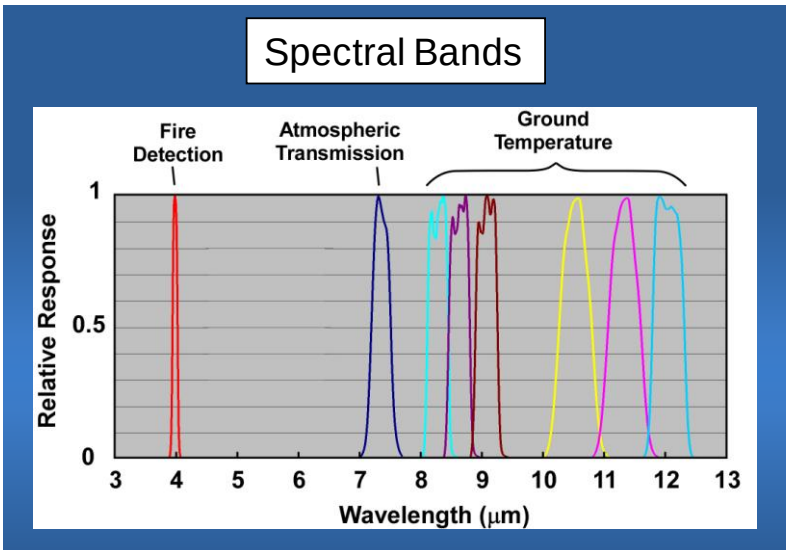

Figure 1. HyspIRI TIR instrument proposed spectral bands.

Table 1. Preliminary TIR Measurement Characteristics

Spectral	
Bands (8) µm	3.98 µm, 7.35 µm, 8.28 µm, 8.63 µm, 9.07 µm, 10.53 µm, 11.33 µm, 12.05 µm
Bandwidth	0.084 µm, 0.32 µm, 0.34 µm, 0.35 µm, 0.36 µm, 0.54 µm, 0.54 µm, 0.52 µm
Accuracy	<0.01 µm
Radiometric	
Range	Bands 2–8 = 200 K–500 K; Band 1 = 1200 K
Resolution	< 0.05 K, linear quantization to 14 bits
Accuracy	< 0.5 K 3-sigma at 250 K
Precision (NEdT)	< 0.2 K
Linearity	>99% characterized to 0.1 %
Spatial	
IFOV	60 m at nadir
MTF	>0.65 at FNy
Scan Type	Push-Whisk
Swath Width	600 km (±25.5° at 623-km altitude)
Cross Track Samples	9,300
Swath Length	15.4 km (± 0.7 degrees at 623 km altitude)
Down Track Samples	256
Band to Band Co-Registration	0.2 pixels (12 m)
Pointing Knowledge	10 arcsec (0.5 pixels) (approximate value, currently under evaluation)
Temporal	
Orbit Crossing	11 a.m. Sun synchronous descending
Global Land Repeat	5 days at Equator
On Orbit Calibration	
Lunar views	1 per month {radiometric}
Blackbody views	1 per scan {radiometric}
Deep Space views	1 per scan {radiometric}
Surface Cal Experiments	2 (day/night) every 5 days {radiometric}
Spectral Surface Cal Experiments	1 per year
Data Collection	
Time Coverage	Day and Night
Land Coverage	Land surface above sea level
Water Coverage	Coastal zone minus 50 m and shallower
Open Ocean	Averaged to 1-km spatial sampling
Compression	2:1 lossless

A key science objective for the TIR instrument is the study of hot targets (volcanoes and wildfires), so the saturation temperature for the 4-µm channel is set high (1200 K) [*Realmuto et al.* 2011], whereas the saturation temperatures for the thermal infrared channels are set at 500 K.

The TIR instrument will operate as a whiskbroom mapper, similar to MODIS but with 256 pixels in the cross-whisk direction for each spectral channel (Figure 2). A conceptual layout for the instrument is shown in Figure 3. The scan mirror rotates at a constant angular speed. It

sweeps the focal plane image across nadir, then to a blackbody target and space, with a 2.2-second cycle time.

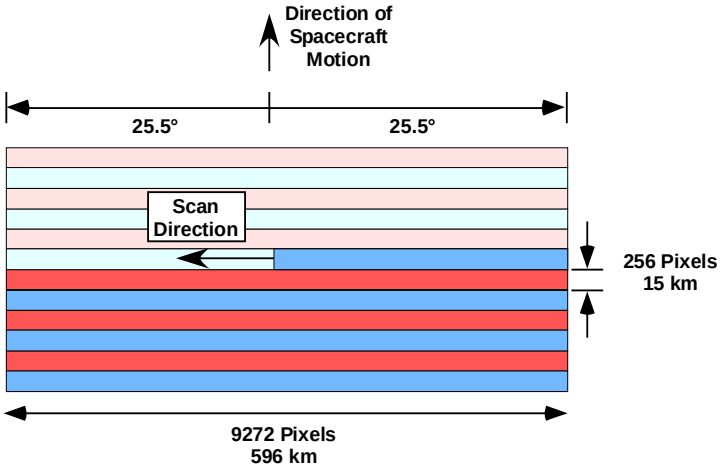

Figure 2. HyspIRI TIR scanning scheme.

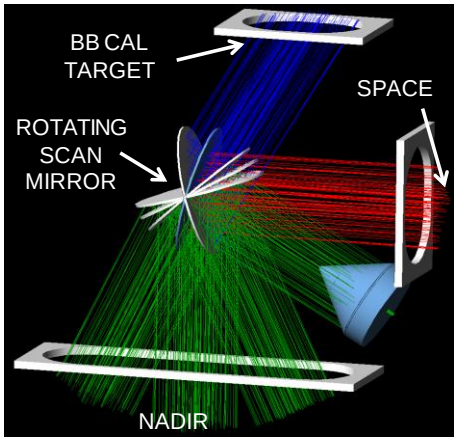

Figure 3. HyspIRI TIR conceptual layout.

The f/2 optics design is all reflective, with gold-coated mirrors. The 60-K focal plane will be a single-bandgap mercury cadmium telluride (HgCdTe) detector, hybridized to a CMOS readout chip, with a butcher-block spectral filter assembly over the detectors. Thirty-two analog output lines, each operating at 10–12.5 MHz, will move the data to analog-to-digital converters.

The temperature resolution of the thermal channels is much finer than the mid-infrared channel, which (due to its high saturation temperature) will not detect a strong signal until the target is above typical terrestrial temperatures at around 400 K. All the TIR channels are quantized at 14 bits. Expected sensitivities of the eight channels, expressed in terms on noise-equivalent temperature difference, are shown in the following two plots (Figures 4 and 5).

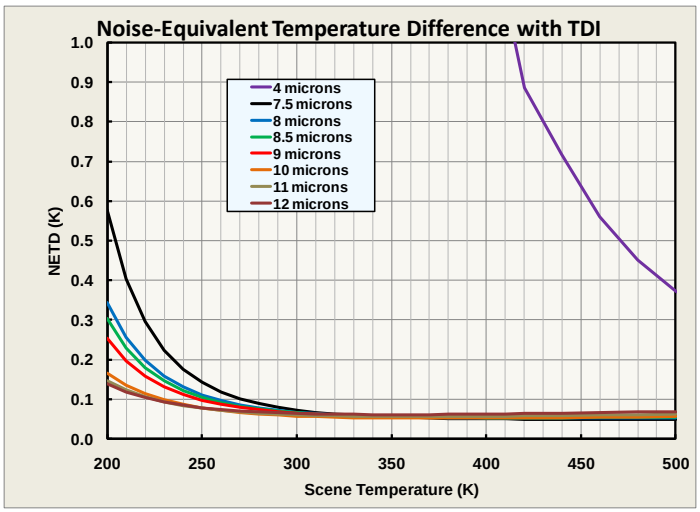

Figure 4. HyspIRI TIR predicted sensitivity 200–500 K.

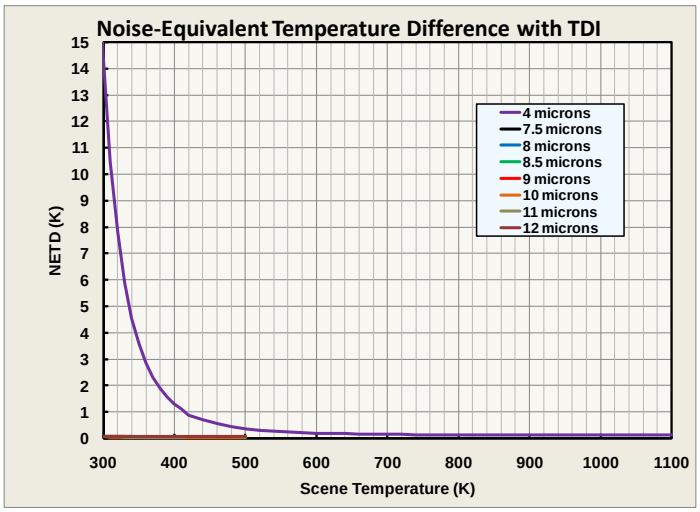

Figure 5. HyspIRI TIR predicted sensitivity 300–1100 K.

The TIR instrument will have a swath width of 600 km with a pixel spatial resolution of 60 m, resulting in a temporal revisit of 5 days at the equator. The instrument will be on both day and night, and it will acquire data over the entire surface of the Earth. Like the VSWIR, the TIR instrument will acquire full spatial resolution data over the land and coastal oceans (to a depth of <50 m) but, over the open oceans, the data will be averaged to a spatial resolution of 1 km. The large swath width of the TIR will enable multiple revisits of any spot on the Earth every week (at least one day view and one night view). This repeat period is necessary to enable monitoring of dynamic or cyclical events such as volcanic hotspots or crop stress associated with water availability.

3 HyspIRI thermal infrared science objectives

The HyspIRI mission is science driven by linking the measurement requirements for the mission to one or more science questions. HyspIRI has three top-level science questions related to 1) ecosystem function and composition, 2) volcanoes and natural hazards, and 3) surface composition and the sustainable management of natural resources [*HyspIRI*, 2008]. The NRC Decadal Survey called out these three areas specifically. These questions provide a scientific framework for the HyspIRI mission. NASA appointed the HyspIRI Science Study Group (SSG) to refine and expand these questions to a level of detail that was sufficient to define the measurement requirements for the HyspIRI mission. Five overarching thematic questions (TQ) were defined by the HyspIRI SSG for the TIR component:

- TQ1: **Volcanoes and Earthquakes**: How can we help predict and mitigate earthquake and volcanic hazards through detection of transient thermal phenomena?
- TQ2: **Wildfires**: What is the impact of global biomass burning on the terrestrial biosphere and atmosphere, and how is this impact changing over time?
- TQ3: **Water Use and Availability**: How is consumptive use of global freshwater supplies responding to changes in climate and demand, and what are the implications for sustaining water resources?
- TQ4: **Urbanization and Human Health**: How does urbanization affect the local, regional, and global environment? Can we characterize this effect to help mitigate its effects on human health and welfare?
- TQ5: **Earth Surface Composition and Change**: What are the composition and thermal properties of the exposed surface of the Earth? How do these factors change over time and affect land use and habitability?

For each of these questions, accurate retrieval of Land Surface Temperature and Emissivity plays a key role in defining the measurement objectives and requirements for these questions. The HyspIRI LST product, in particular, will be especially useful for studies of surface energy and water balance in agricultural regions at the crop scale (<100 m), where quantification of evapotranspiration processes are essential for helping land managers make important decisions relating to water use and availability. The HyspIRI emissivity product will

contain spectral/compositional information from rocks, soils, and vegetation at different wavelengths, which will provide a diagnostic tool for discriminating surface cover types at spatial scales of 60 m or less.

4 Background

In terms of TIR band positions, the HyspIRI TIR measurement will derive its heritage from the ASTER, MASTER, TIMS, and MODIS multispectral measurements. ASTER is a five-channel multispectral TIR scanner that was launched on NASA's Terra spacecraft in December 1999 with a 90-m spatial resolution and revisit time of 16 days. The TIR positions of ASTER bands 10–14 are placed in the so called atmospheric 'window' regions of the TIR region (8–12 µm) and centered on 8.3, 8.6, 9.1, 10.6 and 11.3 µm respectively. These positions allow accurate emissivity surface temperature retrievals which are used for mineralogic composition and mineral mapping studies [*Hook et al.,* 2005; *Vaughan et al.,* 2005; *Scheidt, et al., 2011*]. The ASTER band positions are very similar to the NASA airborne Thermal Infrared Multispectral Scanner (TIMS), which has six spectral channels from 8–12 µm centered on 8.4, 8.8, 9.2, 9.9, 10.7, and 11.6 µm respectively.

MODIS is a multi-spectral imager onboard the Terra and Aqua satellites of NASA's Earth Observing System (EOS), and has been the flagship for land-surface remote sensing since the launch of Terra in December 1999 [*Justice et al.,* 1998]. MODIS scans ±55º from nadir and provides daytime and nighttime imaging of any point on the surface of the Earth every 1–2 days with a spatial resolution of ~1 km at nadir and 5 km at higher viewing angles at the scan edge [*Wolfe et al.,* 1998]. MODIS TIR bands include bands 28 (7.175–7.475 µm), 29 (8.4–8.7 µm), 30 (9.58–9.88 µm), 31 (10.78–11.28 µm), 32 (11.77–12.27 µm) and their placement include key uses such as upper tropospheric humidity, surface temperature, total ozone, cloud temperature, cloud height, and volcano monitoring. The MODIS/ASTER Airborne Simulator (MASTER) was developed to support scientific studies by ASTER and MODIS projects, including algorithm development and band placement studies [*Hook et al.,* 2001]. At present, the nominal HyspIRI TIR band placements are a hybrid between ASTER and MODIS TIR bands, and include MODIS bands 28, 32 and ASTER bands 10–12 shown in Figure 6.

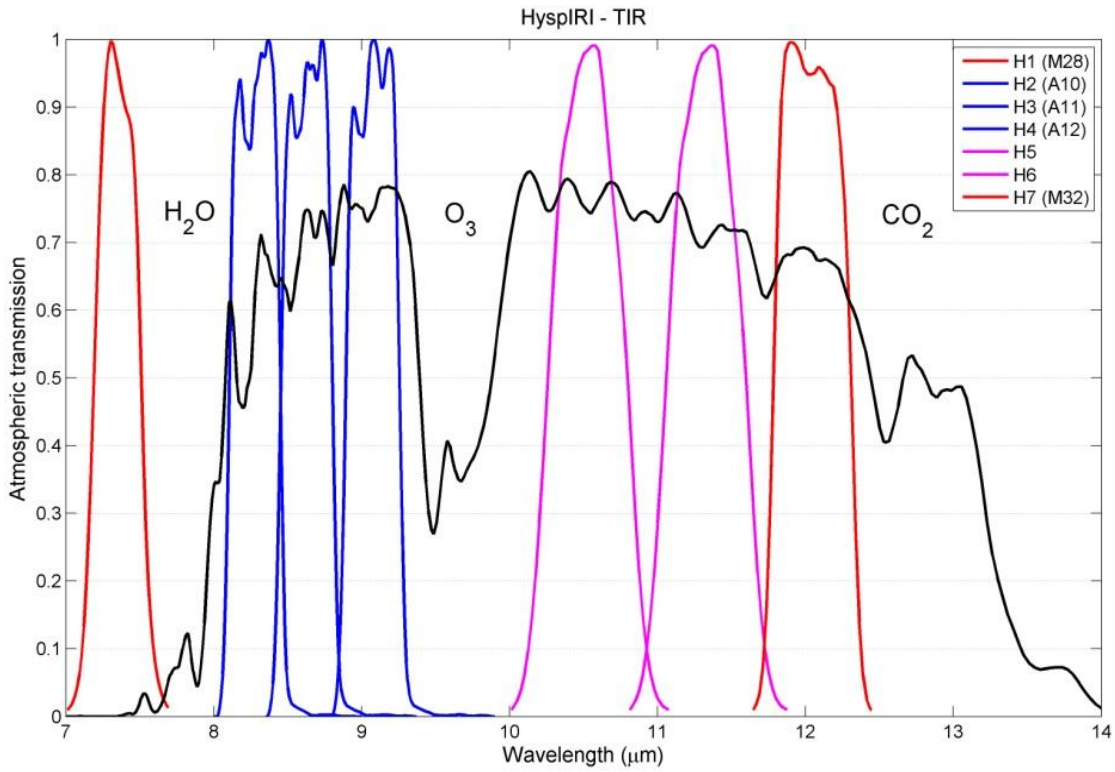

Figure 6. HyspIRI nominal band positions in the TIR region based on MODIS bands 28 and 32 (H1 and H7), and ASTER bands 10–12 (H2–H4). Bands H5 and H6 centered at 10.53 and 11.33 micron are similar to ASTER bands 13 and 14. Transmission features of H_2O, O_3 and CO_2 are also shown as reference.

The TQ1 HyspIRI overarching science question states: How can we help predict and mitigate earthquake and volcanic hazards through detection of transient thermal phenomena? It has been shown that transient thermal anomalies precede earthquakes and volcanic eruptions. TIR images from HyspIRI will allow us to monitor these phenomena in the hope of one day providing capability of predicting such disasters. Precursory behaviors of volcanoes can include increases in SO_2 emission, and therefore TIR data will allow us to detect not only SO_2, but also ash and water ice in the eruptive plumes [*Realmuto and Worden*, 2000; *Realmuto et al.*, 1997]. Similarly, thermal anomalies such as crater lakes, fumaroles, domes, etc. typically precede an eruption [*Ramsey and Harris, 2012; Rosi et al., 2006*]. Remote monitoring of this activity provides crucial information that can lead to more accurate event predictions. SO_2 absorption primarily occurs in the 7.5 and 8.5 μm regions, and correct placement of bands around these regions is essential for quantitatively mapping SO_2 plumes.

Figure 7 (a) shows an ASTER nighttime multispectral TIR image of Augustine Volcano on 1 February 2006 showing hot pyroclastic flow deposits (bright in TIR) and eruption plume.

Colors represent different materials entrained within plume. For example, magenta indicates mixtures of water droplets (steam) and silicate ash; red, yellow, and orange indicate mixtures of ash and SO_2. Figure 7 (b) shows an SO_2 map of column abundance derived from ASTER data. The rapid acquisition of the high-resolution ASTER image was possible because of an integrated program of thermal anomaly detection, which uses lower spatial/higher temporal resolution TIR instruments to trigger ASTER TIR observations at a much higher temporal frequency [*Duda et al., 2009*]. HyspIRI will provide both the high spatial and temporal TIR data to make this type of fire and volcano monitoring routinely possible.

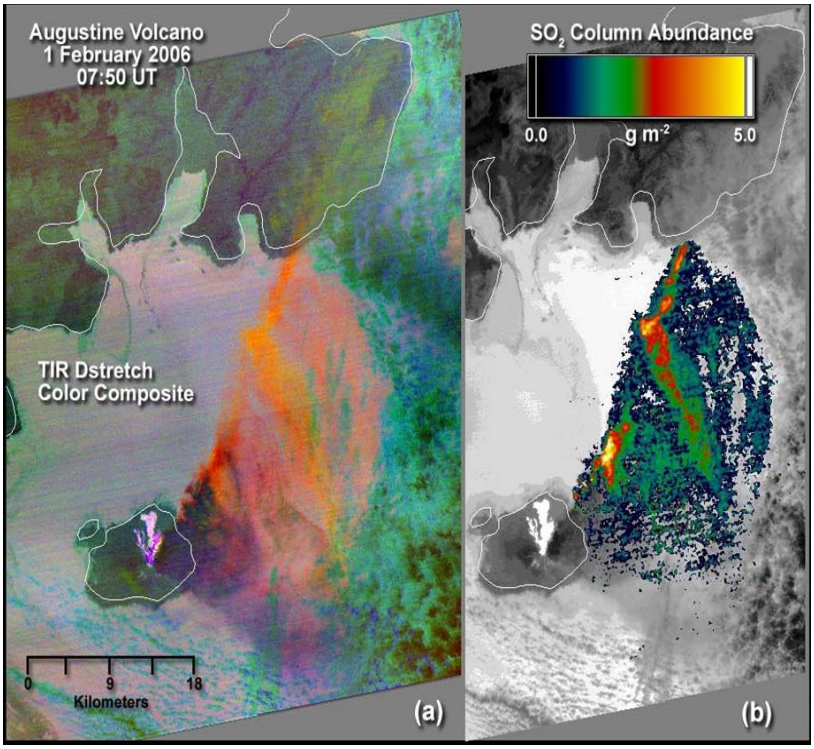

Figure 7. (a) ASTER nighttime TIR images of Augustine Volcano showing hot pyroclastic flow deposits (Bright in TIR) and eruption plume. Colors represent different materials entrained within plume. (b) SO_2 map derived from ASTER data.

The TQ5 HyspIRI overarching science question states: What are the composition and thermal properties of the exposed surface of the Earth, and how do these factors change over time and affect land use and habitability? The emissivity of the exposed terrestrial surface of the Earth can be uniquely helpful in discriminating between different rock, mineral, and soil types. Surface compositional studies hold clues to the origins of materials, the processes the transport/alter these materials, and also the geology and evolution of different rock types. Spaceborne measurements from HyspIRI will enable us to derive surface temperatures and

emissivities for a variety of Earth's surfaces. For example, different Si-O bonded structures vary in their interaction with energy in the thermal infrared region (8–12 μm). Framework silicates, such as quartz and feldspar (common in most continental rocks), show minimum emissivity at shorter wavelengths (8.5 μm), whereas pyroxene and olivine (common in many volcanoes) show minimum emissivity at progressively longer wavelength. Carbonate minerals have a diagnostic feature around between 11.2 and 11.4 μm, which moves from the shorter to the longer wavelengths as the atomic weight of the cation increases. Correct placement of the TIR bands in the 8–12 μm is critical for mapping and distinguishing between felsic and mafic rock compositions as well as positively identifying certain minerals, mineral classes, and urban materials. Figure 8 shows an example of an ASTER-derived decorrelation stretch (DCS) over Death Valley, CA. The DCS exploits inter-channel differences to enhance the color in images, resulting in an image where the pixels are distributed among the full range of possible colors. ASTER bands 14, 12, and 10 are plotted as red, green, and blue (RGB), respectively. Quartz-rich rocks are displayed in red and magenta, quartz-poor rocks in blues and purples, and carbonates in green. Temperature information is related to the brightness of the colors, i.e., areas of higher elevation (and cooler rocks) appear darker than lower elevation areas that have higher temperatures.

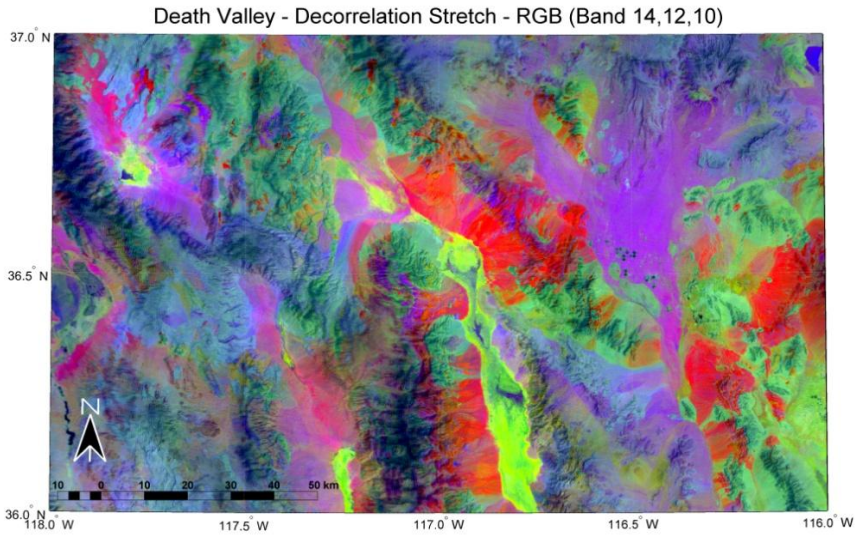

Figure 8. ASTER decorrelation stretch (DCS) of Death Valley using bands 14, 12, and 10 as RGB respectively. Different colors in the image correspond to different mineral types, e.g., quartz features are red, carbonates are green, and quartz-poor regions are purple.

5 HyspIRI band positions for the detection of volcanic plumes

TIR data will allow us to measure the emission rates of SO_2 from volcanoes. This in turn allows us to infer magma supply rates, contributions of volcanoes to the global SO_2 budget and emission rates of other amounts of gas (e.g., H_2O, CO_2, HCL, HF) and aerosols (ash, ice, sulfates) [*Realmuto et al.,* 1997; *Watson et al.,* 2004]. The frequent coverage and the higher spatial resolution of HyspIRI will allow us to more-accurately monitor passive SO2 degassing from the world's active volcanoes. This input of emissions into the troposphere will affect local and regional climate around these persistently-active volcanoes, a capability not offered by existing moderate (~1 km) resolution instruments. Multispectral TIR data will also allow the identification of the mixture of ash, SO_2, and water vapor/ice in eruptive plumes, providing improved hazards warnings for aviation safety [*Realmuto and Worden*, 2000; *Tupper et al.*, 2006].

The use of multispectral TIR airborne data to map volcanic SO_2 plumes has been previously demonstrated with much success [*Realmuto et al.,* 1997; *Realmuto et al.,* 1994]. With the launch of NASA's Terra spacecraft in 1999, volcanic plume monitoring is now possible twice daily with MODIS data and at much higher spatial resolution with ASTER data. For example, MODIS will have sufficient resolution to monitor large-scale SO_2 plumes typical of those seen from Kilauea in Hawaii or Mount Etna in Italy [*Realmuto et al.,* 1994]. In contrast, ASTER has the ability to resolve smaller-scale plumes such as those from Pacaya in Guatemala or Soufrière Hills in Montserrat. Algorithms for detecting plumes rely on spectral attenuation of infrared radiation between 7–13 μm. ASTER band 11 and MODIS band 29 can be used to detect SO_2 burdens, whereas the 11-12 micron split-window bands can quantify silicate ash and water ice. The clarity of the Earth's atmosphere in these regions allow the detection of these plume constituents down to ground level. In contrast, the 7.3 micron absorption for SO_2 is much stronger, but is only effective if the plume is very large and/or enters the stratosphere due to the strong absorption of water vapor in this region. The heritage of the HyspIRI spectral response versus SO_2 transmission is shown in Figure 9, including the ASTER and MODIS band passes.

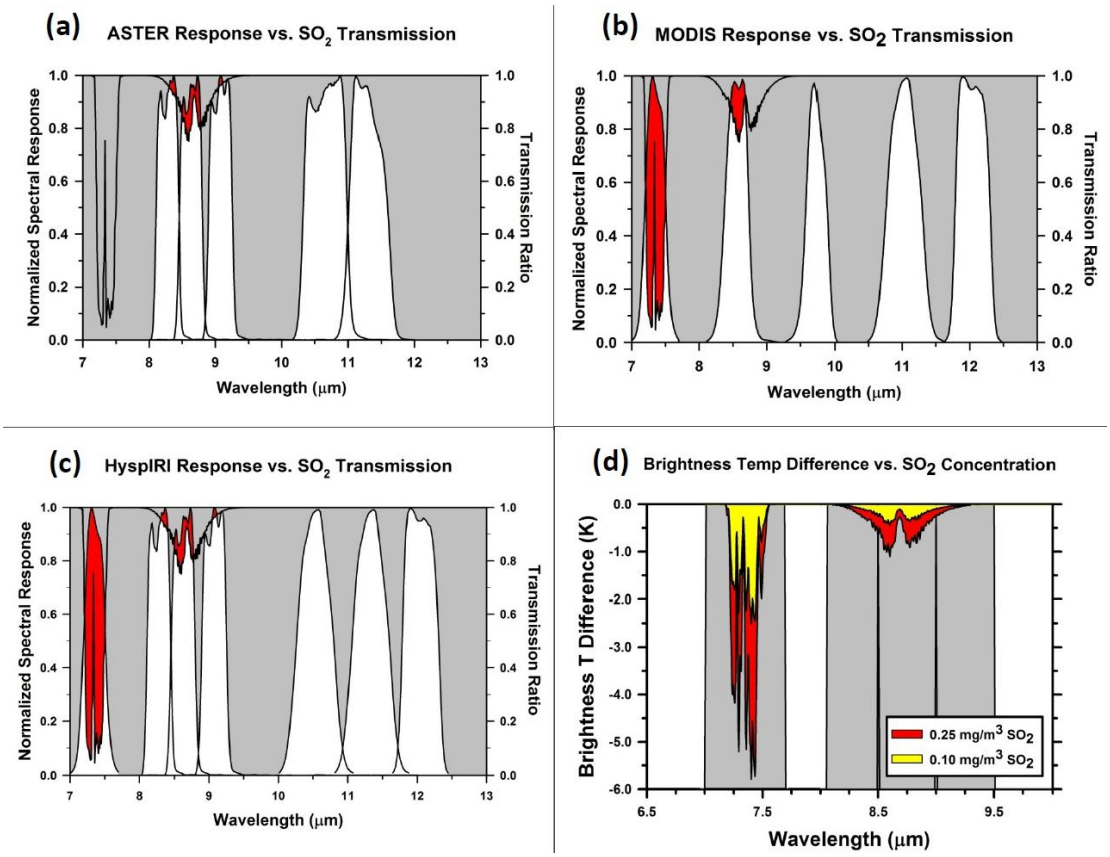

Figure 9. Heritage of the HyspIRI spectral response, showing (a) ASTER response vs. SO_2 transmission, (b) MODIS response vs. SO2 transmission, (c) HyspIRI response vs. SO_2 transmission, and (d) brightness temperature difference vs. SO_2 concentration.

The retrieval of SO_2 concentrations from remote-sensing measurements relies on radiative transfer models that estimate the amount of atmospheric emission, and scattering and absorption of surface-leaving radiance. The recent introduction of high-resolution (0.1 cm^{-1}) band models in MODTRAN5 [*Berk et al.*, 2005] enables us to analyze hyperspectral TIR data. Hyperspectral radiance measurements improve our ability to discriminate the constituents of volcanic plumes. A limitation of radiative transfer models are their dependence on input atmospheric profiles such as temperature, relative humidity, and gas composition. Furthermore, the need for accurate atmospheric corrections increases with increasing spectral resolution. The improvement in our ability to model ambient atmospheric conditions, and thus improve atmosphere corrections, will increase our sensitivity to subtle changes in passive emissions of SO_2 and surface temperature, regardless of the spectral resolution of our radiance measurements.

5.1 Mapping volcanic plume constituents

Comparisons between multi- and hyperspectral remote sensing in the detection and mapping of plume constituents are illustrated in Figure 10, which shows the spectral signatures of SO_2 (Figure 10a), silicate ash (Figure 10b), and SO_4 aerosol (Figure 10c). These simulated spectra are plotted at the resolution of HyTES [*Johnson et al.*, 2009] and the airborne MODIS/ASTER Airborne Simulator, or MASTER [*Hook et al.*, 2001] instruments: ~0.02 μm (or 2 cm-1) vs. 0.5–1.0 μm, respectively. In comparison, the thermal IR response of these corresponding constituents is shown on the right panels in Figure 10. We can readily

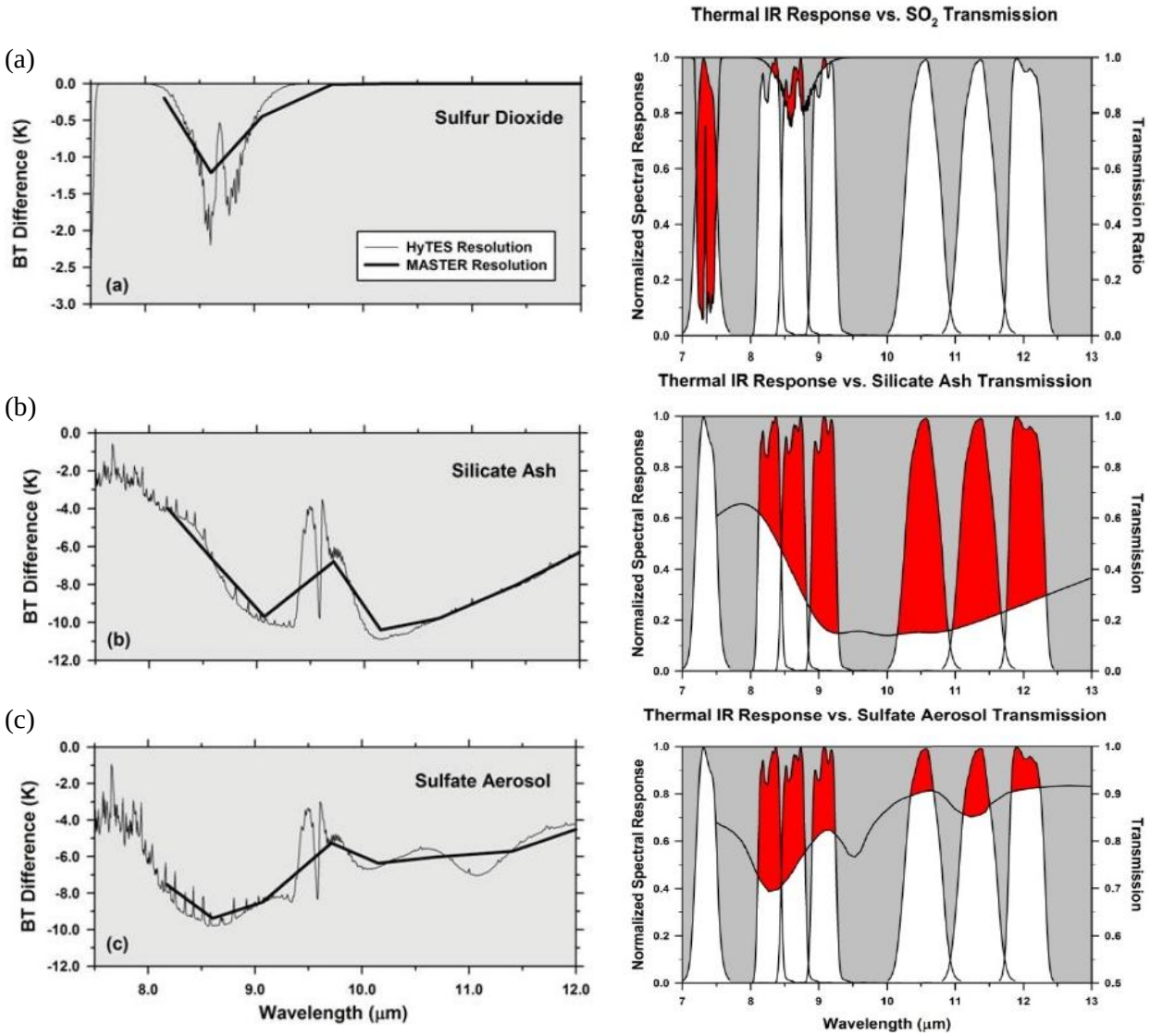

Figure 10. Transmission spectra expressed as brightness temperature difference spectra for three constituents of volcanic plumes and ash clouds. (a) SO_2, (b) silicate ash, and (c) SO_4 aerosol at the spectral resolution of HyTES (thin line) and MASTER (thick line)

discriminate the spectra of SO_2, ash, and SO_4 aerosols at the spectral resolution of HyTES (thin line), but the distinctions are more subtle at the resolution of MASTER (thick line). In real-world measurements, these distinctions are further muted by instrument noise and uncertainties in our knowledge of atmospheric and surface conditions. Given the MASTER spectra, we note the difficulties in discriminating SO_2 from SO_4 in the spectral range between 8 and 9.5 μm (Figures 10a and 10c), or ash from SO_4 in the range between 9.5 and 12 μm (Figures 10b and 10c).

The ability to discriminate SO_4 aerosols from SO_2 or ash is critical for climate and environmental studies; whereas the ability to discriminate ash from SO_4 (or SO_2) is critical to the mitigation of the aviation hazards posed by drifting ash clouds [*Prata et al.*, 2001; *Tupper et al.*, 2006].

5.1.1 Conclusions

SO_2 transmission in the longwave region (12–11 μm absorption difference) can be confused with sulfate aerosols and/or ash with current band positions. A suggestion would be to shift the HyspIRI 10.53 μm band between 9.5 and 10 μm in order to help discriminate sulfate aerosols from SO_2 or ash. Simulations will need to be run to investigate the effects of O_3 absorption in this region, and optimal placement of the 10.53 μm band. In terms of mineral mapping, moving the 10.53 μm band closer to 10 μm will also help to discriminate between feldspar and quartz minerals. This will be discussed in more detail in section 6. In any case, moving the 10.53 μm band to shorter wavelength region around the 10 μm band will be beneficial for both SO_2 and mineral mapping techniques.

5.2 Case Study: Mount Etna eruption plume

5.2.1 Analysis

Figure 11 shows a MODIS-Aqua visible (top) and thermal (bottom) image of a Mount Etna plume on the 28 Oct 2002 using band 28 (7.3 μm). The ground is not visible because at this wavelength the atmosphere is opaque due to strong H_2O and SO_2 absorption features. This is illustrated in Figure 11 (right panels) which shows that H_2O and SO_2 absorption strengths are of similar magnitude in the 7.3 μm band. This makes it difficult to separate their effective contributions to the total brightness temperature. In addition the 7.3 μm band is not suitable for mapping plumes below 5 km, and is therefore more useful for mapping large-scale eruptions where plumes persistent to higher altitudes in the stratosphere.

5.2.2 Conclusions

A more useful option for HyspIRI would be to move the 7.3 µm band closer to the 7.8–8 µm region in order to obtain more leverage from the water vapor absorption gradient that exists in this range (see Figure 11 top right panel). This would make simultaneous retrievals of SO_2 and H_2O easier in combination with the 8.6 µm SO_2 absorption feature.

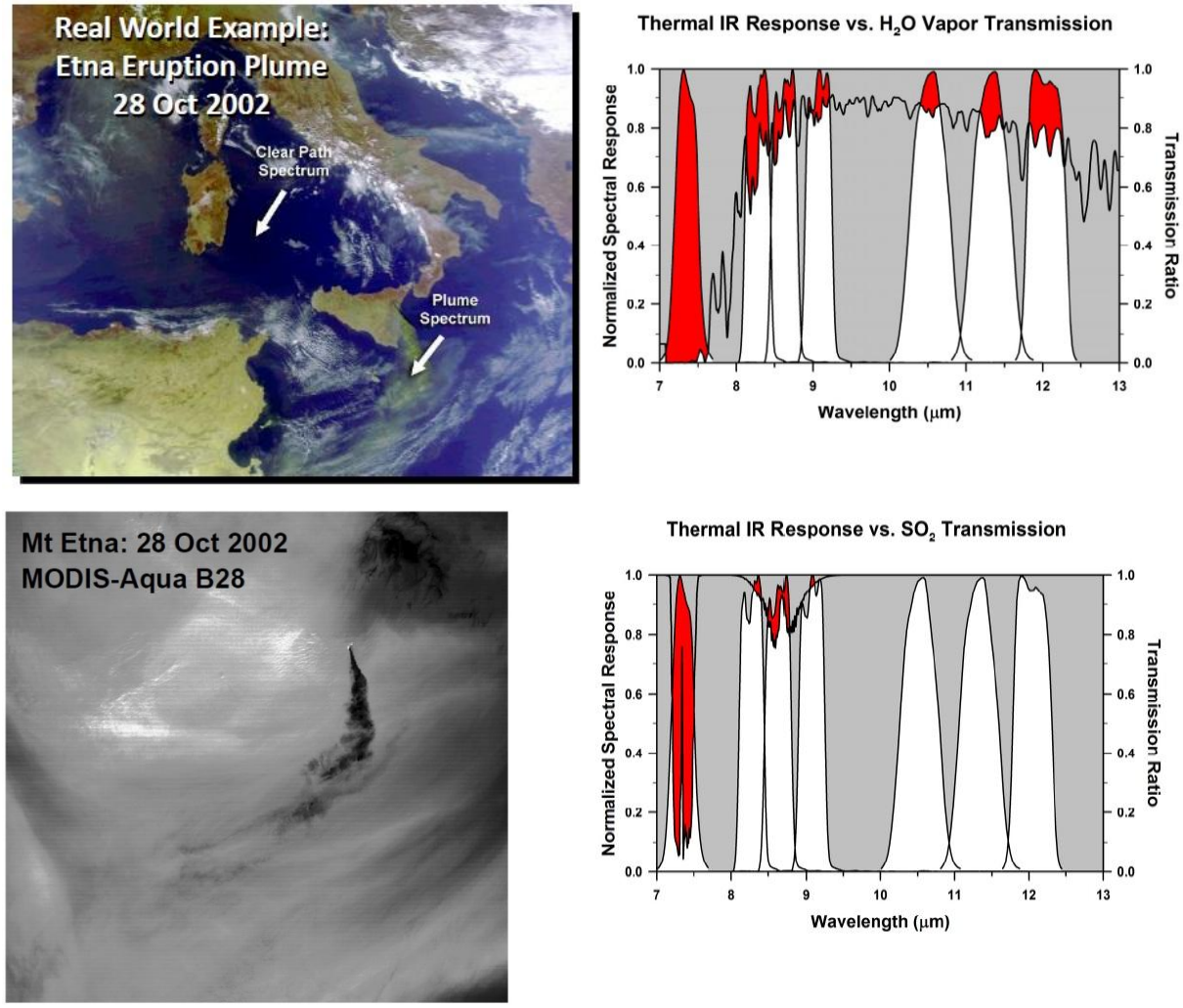

Figure 11. (left) MODIS-Aqua band 28 (7.3 µm) image of the Mount Etna eruption on 28 October 2002, (right) thermal infrared responses of HyspIRI plotted with transmission curves for water vapor (top) and SO_2 (right).

5.3 Case Study: Sarychev Peak volcano

5.3.1 Analysis

Figure 12 illustrates the complex dispersion of plumes and clouds during the recent eruptions of Sarychev Peak Volcano (Matua Island, Russian Kuril Islands). Figure 12(a) top panel is a true-color composite of MODIS-Terra data acquired at 00:50 UTC on 16 June 2006. We note the viewing conditions were cloudy, indicating unstable atmospheric conditions, and the

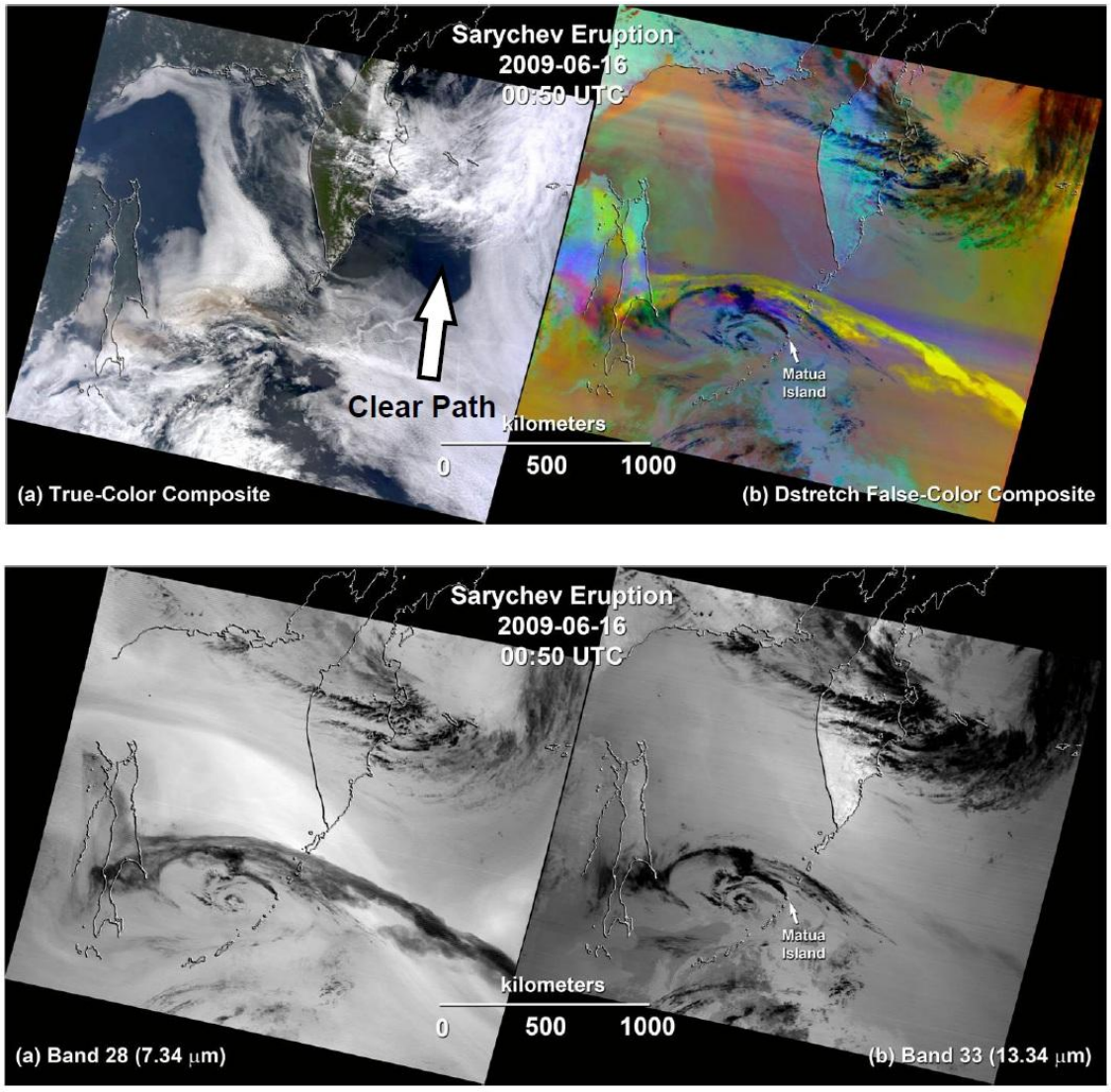

Figure 12. Eruption of Sarychev Peak Volcano (Matua Island, Russian Kuril Islands). Top panels (a) true-color composite of MODIS-Terra data acquired at 00:50 UTC on 16 June 2006. (b) is a false-color composite of MODIS thermal infrared (TIR) channels 32, 31, and 29 displayed in red, green, and blue, respectively. Bottom panels show corresponding (a) MODIS band 28 (7.34 μm) and (b) band 33 (13.34 μm) brightness temperatures.

eruption plume was obscured by the meteorological (met) clouds. Figure 12(b) top panel is a false-color composite of MODIS thermal infrared (TIR) channels 32, 31, and 29 displayed in red, green, and blue, respectively.

The radiance data were processed with the DCS. Due to distinctive features in the spectra of SO_2 and silicate ash [*Watson et al.*, 2004], SO_2-rich clouds appear yellow and ash-rich plumes and clouds appear in hues of red and purple. The portions of the volcanogenic and met clouds that are opaque to TIR radiance appear dark in Figure 12(b), signifying low radiometric temperatures.

The retrieval procedure for SO_2 requires profiles of atmospheric temperature, H_2O and O_3 as input to a radiative transfer model such as MODTRAN [*Kneizys et al.*, 1996]. Radiance spectra from a clear path (plume-free) shown in Figure 12(a) are used to first 'tune' the H_2O and O_3 profiles. Depending on the conditions, considerable spatial variations of H_2O within a scene may be present, which makes tuning a time-consuming process. Two candidate regions for better characterizing the H_2O distribution within a scene include the MODIS band 28 (7.34 µm) and band 33 (13.34 µm) channel. The brightness temperature plots in Figure 12(a) and (b) bottom panels show that strong H_2O absorption in the MODIS band 28 channel obscures the surface features, while in band 33, moderate H_2O absorption does not obscure the surface.

5.3.2 Conclusions

The 7.3 µm channel does not provide sufficient resolution to separate the effects of H_2O and SO_2 absorptions, despite the original proposal to add this channel for SO^2 detection and mapping. Characterizing spatial variations in H_2O within a scene will help to optimize the SO_2 retrievals and allow us to better characterize the atmosphere regardless of the ground target. For HyspIRI it is suggested to shift the 7.3 µm band closer to the 7.8–8 µm region in order to obtain more leverage from the water vapor absorption gradient that exists in this range, but a more definitive solution to the exact position requires higher spectral resolution data, such as HyTES and MAGI (see section 7). Adopting a longer wavelength band (e.g., MODIS band 33) for plume mapping will not be necessary for HyspIRI due to the three bands already positioned in the 8–9 µm SO_2 absorption feature.

6 HyspIRI band positions for Earth surface compositional mapping

Surface compositional studies hold clues to the origins of materials and also the geology and evolution of different rock types. Spaceborne measurements from HyspIRI will enable us to derive surface temperatures and emissivities of a variety of Earth's geologic surfaces. For example, different Si-O bonded structures vary in their interaction with energy in the thermal infrared region (8–12 μm). Framework silicates, such as quartz and feldspar, show minimum emissivity at shorter wavelengths (8.5 μm), whereas olivine and pyroxene minerals show minimum emissivity at progressively longer wavelengths [*Hunt*, 1980].

Primary rock-forming minerals exhibit major and diagnostic spectral absorption features in the infrared wavelength region of the electromagnetic spectrum, with only minor features in the visible/shortwave (VSWIR) infrared region (Figure 13). These features result from the selective absorption of photons with discrete energy levels and are dependent on the elemental composition, crystal structure, and chemical bonding characteristics of a mineral, and are therefore diagnostic of mineralogy [*Hunt*, 1980; *Vaughan et al.*, 2005]. For example, different Si-O bonded structures vary in their interaction with energy in the thermal infrared region (8-12 μm). Examples of reflectivity measurements from the ASTER spectral library (ASTlib) are shown in Figure 13 for six different rock types including metamorphic, sedimentary and igneous. The left panels show the VSWIR spectral range, whereas the right panels show the mid to-thermal infrared spectral range. The thermal spectra show original full resolution ASTlib spectra (solid lines) [*Baldridge et al.*, 2009] overlaid with the eight convolved HyspIRI preliminary TIR band placements (black circles). ASTlib includes spectra of rocks, minerals, terrestrial soils, lunar soils, manmade materials, vegetation, snow, and ice, covering spectral ranges from the visible to longwave infrared (0.4–15.4 μm).

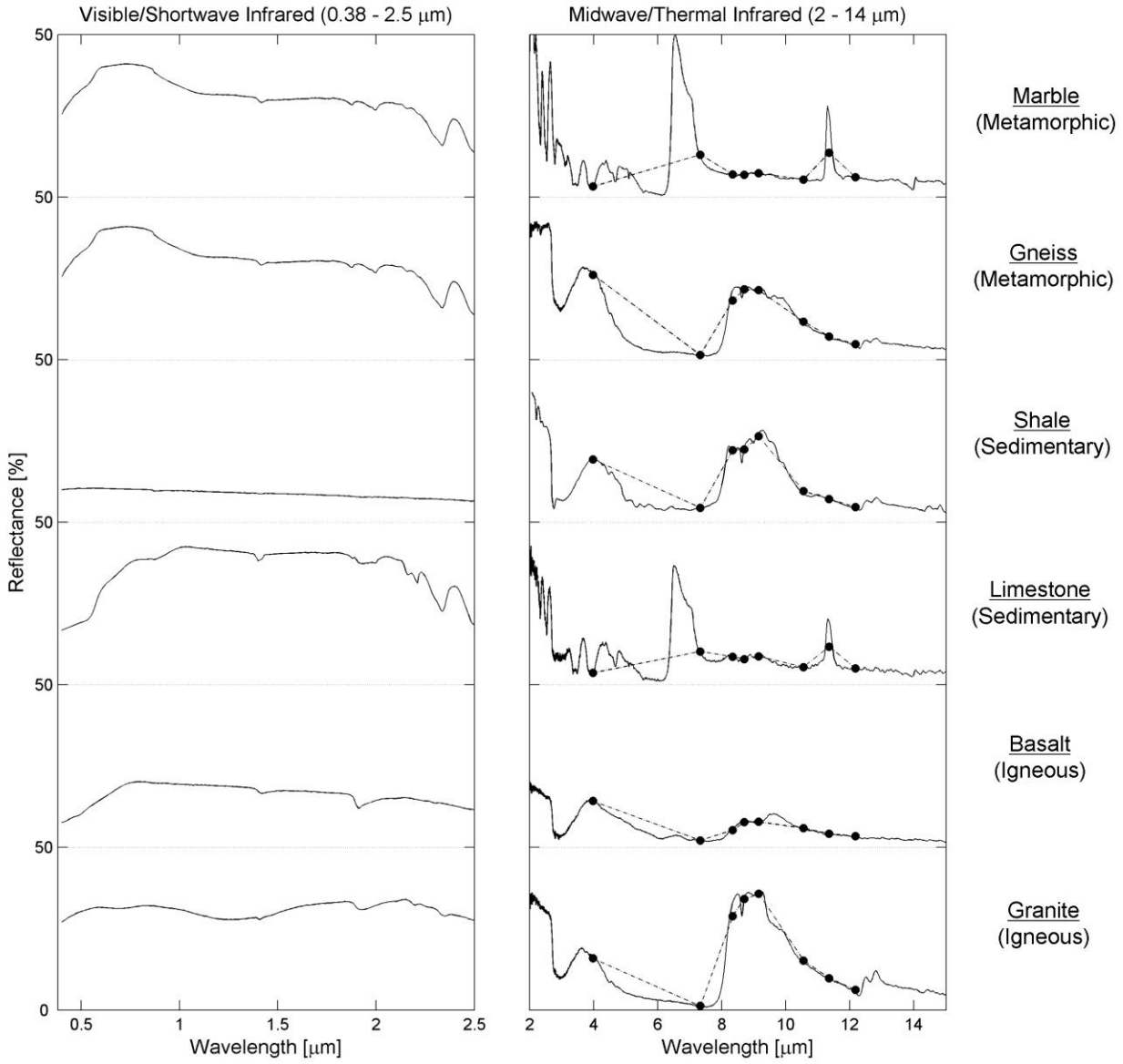

Figure 13. A selection of JPL mineral library spectra representing several classes shown as percent reflectance in the visible, shortwave infrared (0.38–2.5 μm) and infrared (2–14 μm) regions. Black circles in the infrared spectrum represent HyspIRI bands convolved to the library spectra. All spectra are offset for clarity.

The spectral features illustrated in Figure 13 result from the minerals that occur in these felsic to mafic igneous rock types. For example, emissivity minimums occur at 8.3 and 9.1 μm for granite, shale, and gneiss, whereas for basalt this feature is more subdued and shifted to longer wavelengths. Fundamental vibration modes for the CO_3 ion occur throughout the TIR region; in carbonate minerals (e.g., limestone in Figure 13), the most distinguishing features occur around 6.7 μm and 11.3 μm, with the former lying outside of the atmospheric window.

6.1.1 Case Study: Kelso Dunes

The Kelso Dunes are located in the Mojave National Preserve southeast of Baker, California. Sand from the Mojave River alluvial apron is driven approximately 35 miles by predominantly westerly winds, piling up at the base of the Granite and Providence mountains, which flank the south and southeast sides of the dune field. The westerly winds are counterbalanced by strong winds from other directions that result in a result in a variety of dune forms. The dune field covers an area of 115 km^2 and contains dunes that rise up to 195 m above the terrain. Large portions of the dunes have sparse vegetation cover that stabilizes areas of previously drifting sand. The dunes are composed predominately of quartz and feldspar eroded from granitics of San Bernardino Mountains to the south, but also contain a large proportion of lithic fragments [*Edgett and Lancaster*, 1993]. A later study by *Ramsey et al.* [1999] using TIMS data showed significant spectral variations within the active dunes, indicative of potential mineralogic heterogeneities, which was confirmed from results with a linear spectral retrieval algorithm. Further, petrographic techniques showed that the dunes were much less quartz rich than previously reported (90–100% quartz), indicating a more immature dune system than previously thought due to relatively higher percentages of feldspar minerals.

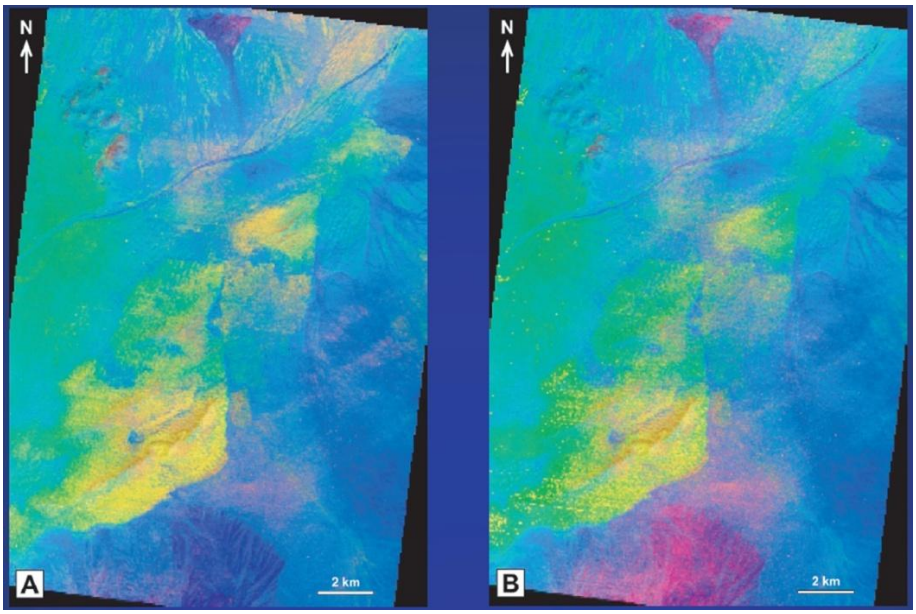

Figure 14. Decorrelation stretch (DCS) images of the Kelso Dunes, CA using MASTER data. The yellow indicates an equal abundance of quartz and microcline feldspar, while cyan is quartz and oligoclose feldspar. Increased magenta coloration in (B) shows improved feldspar detection using the 10.1 µm band instead of the 10.6 µm MASTER band.

Figure 15 shows TIR emissivities of four mineral end-members acquired at Arizona State University including oligoclase, clay+magnetite, quartz, and microcline together with one spectrum (sample k24) of æolian sand from the Kelso Dunes [*Ramsey and Rose*, 2009]. The

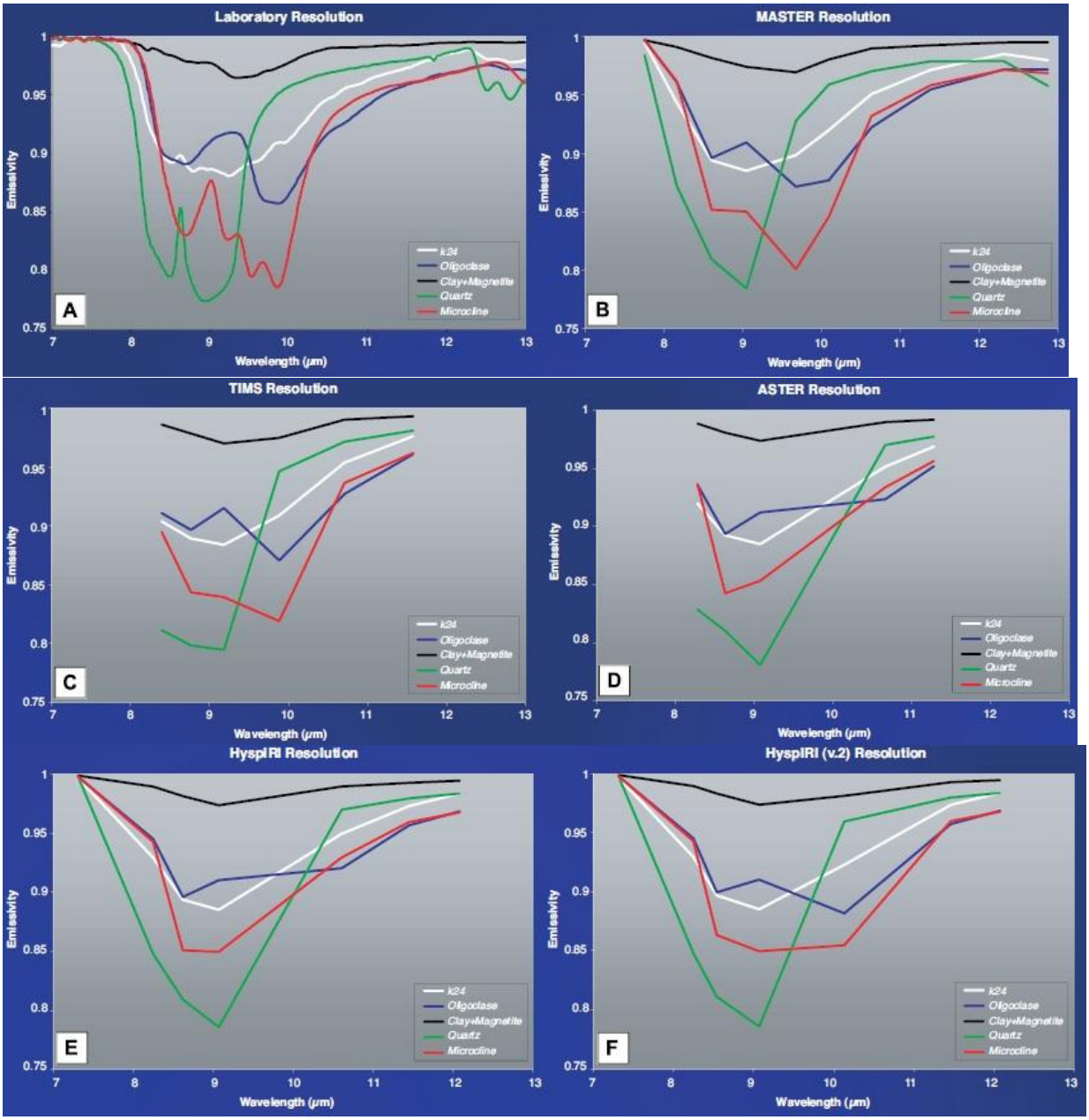

Figure 15. Thermal infrared (TIR) emissivity spectra of four mineral end-members acquired at Arizona State University (Oligoclase, Clay+Magnetite, Quartz and Microcline) and one spectrum (sample k24) of æolian sand from the Kelso Dunes (Mojave Desert, CA). The spectra were degraded to the resolution of various TIR instruments: (A) Laboratory resolution (B) MASTER resolution (10 bands) (C) TIMS resolution (6 bands) (D) ASTER resolution (5 bands) (E) Current HyspIRI resolution (7 bands) and (F) Proposed new HyspIRI band alignment (7 bands). In this configuration, three of the bands have been moved for better gas and mineral detection. The 8.63 µm band has been shifted to 8.55 µm (centered over the SO_2 absorption doublet). The 10.53 µm band has been moved to 10.05 µm for better detection and discrimination of feldspar minerals. The 11.33 µm band has been shifted slightly to 11.35 µm for more accurate carbonate detection.

spectra were degraded to the resolution of various TIR instruments and used to analyze the compositional variation of the Kelso æolian system and argue for a more immature dune system because of the relatively high percentages of feldspar minerals. These include: (A) laboratory resolution; (B) MASTER resolution (10 bands); (C) TIMS resolution (6 bands); (D) ASTER resolution (5 bands); (E) current HyspIRI resolution (7 bands); and (F) a proposed new HyspIRI band alignment (7 bands). In the new proposed HyspIRI band configuration, three of the bands have been moved for better gas and mineral detection. The 8.63 µm band has been shifted to 8.55 µm (centered over the SO_2 absorption doublet), whereas the 10.53 µm band has been moved to 10.05 µm for better detection and discrimination of feldspar minerals. Lastly, the 11.33 µm band has been shifted slightly to 11.35 µm for more accurate carbonate detection. These modifications are highlighted in Figure 16 showing the band position changes in red. Of note in Figure 15(F) is the shape of the microcline and oligoclase feldspar spectra. The lower emissivity at 10.05 microns allows this class of minerals to be clearly distinguished from quartz, which is critical for accurate compositional analysis of geologic and urban surfaces.

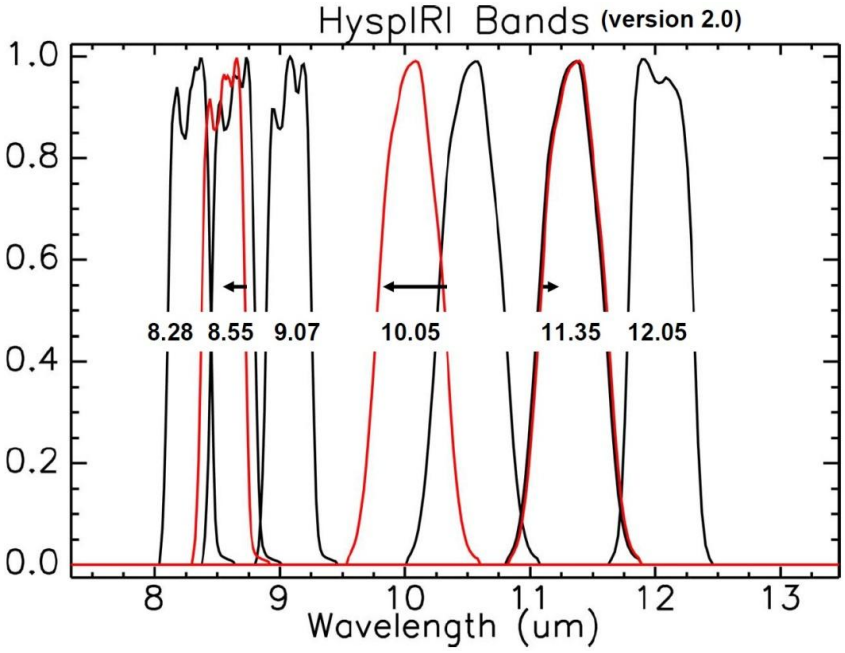

Figure 16. Proposed HyspIRI version 2.0 band locations. Band modifications from version 1.0 are highlighted in red. The 8.63 µm band has been shifted to 8.55 µm, the 10.53 µm band has been moved to 10.05 µm, and the 11.33 µm band has been shifted slightly to 11.35 µm (see text for details).

A method known as spectral deconvolution was then used to assess the ability of each band configuration to resolve the relative abundances of each mineral end member. The accurate

retrieval of mineralogy and abundance from surface materials requires the knowledge of how the radiated energy from each surface component interacts, as well as a model (spectral deconvolution) to separate that mixed energy for each end member [*Ramsey and Christensen*, 1998; *Ramsey et al.*, 1999]. This method relies on input end-member spectra to perform a best fit to the unknown (mixed) spectrum. The output is and a set of corresponding fractions, or abundances, that indicate the proportion of each end member present in the pixel. Analysis of Figure 15 using results of a linear deconvolution algorithm showed that the HyspIRI v2.0 band positions had the best agreement with laboratory derived end member percentages (Figure 17), with a lowest average error of 1.9%. The next closest match was MASTER, followed by ASTER, HyspIRI v1.0, and TIMS.

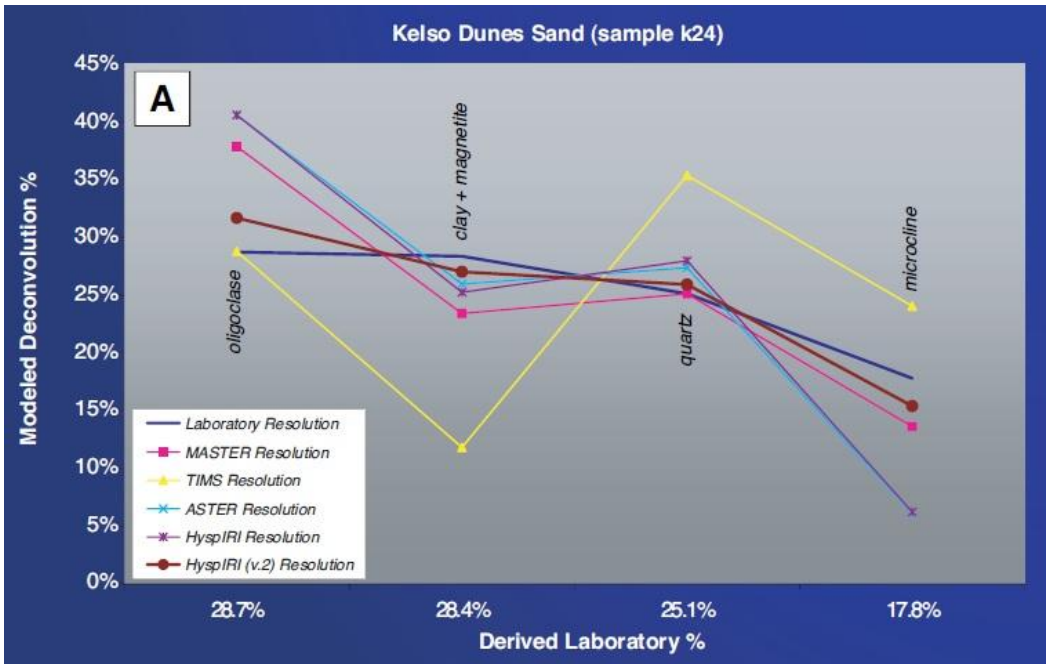

Figure 17. Results of linear deconvolution of the Kelso sand sample (k24) at the various spectral resolution/band configurations shown in Fig 15. The laboratory resolution is assumed to be the most accurate and plotted as the dark blue line for each of the four mineral end-members. The closest match between the laboratory results and the other configurations are for the proposed new HyspIRI version 2.0 spectral bands shown in red (avg. error = 1.9%).

Figure 18 shows laboratory emissivity spectra of different silicate minerals including andesine, anorthoclase, microcline, and quartz, with the current HyspIRI v1.0 band positions highlighted with blue vertical lines. From this image, it is clear that the current 10.53 µm band, situated longward of the ozone absorption features (~9.6 µm) has marginal spectral variation for most silicate minerals including quartz and feldspars. This spectral variation reduces even more if these constituents are mixed, which is commonly the case for æolian dune systems.

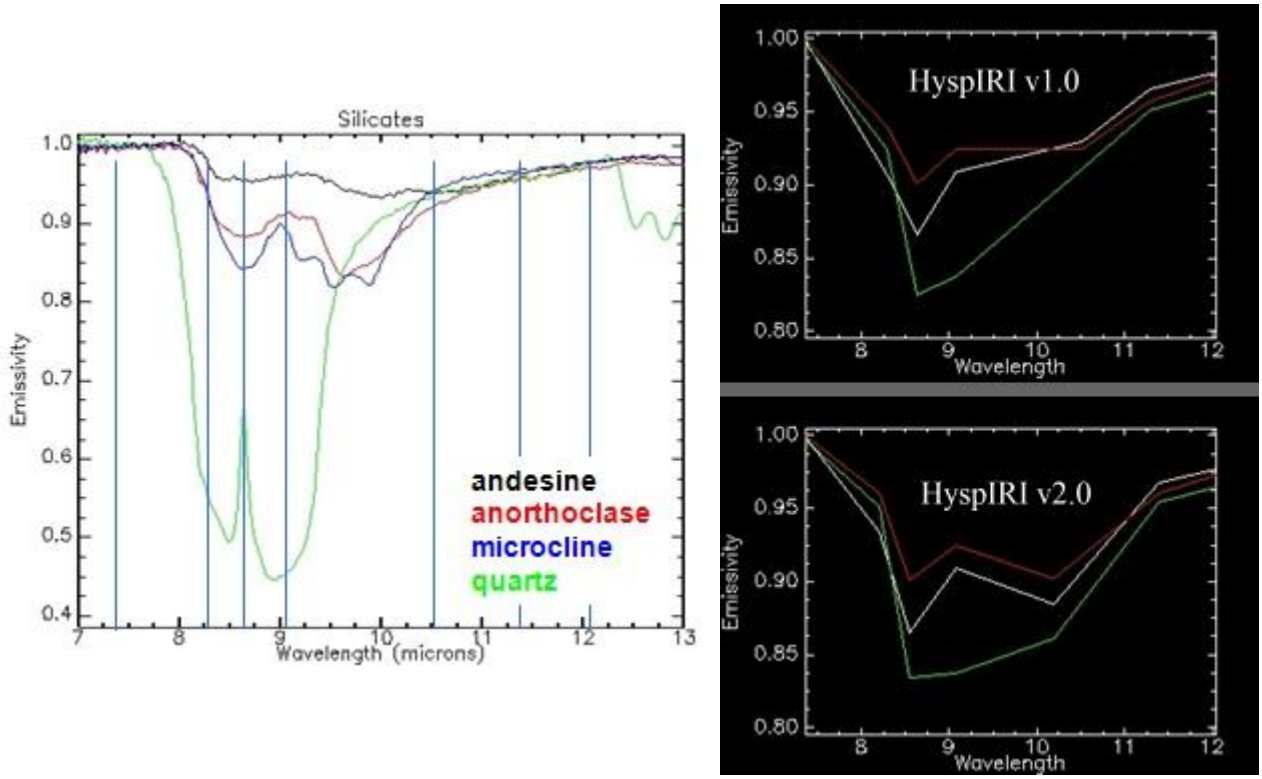

Figure 18. (left) Laboratory emissivity spectra of different silicate minerals including andesine, anorthoclase, microcline, and quartz, (right) silicate spectra convolved to HyspIRI v1.0 and v2.0 band positions.

The emissivity spectra on the right of Figure 18 show the silicate spectra convolved to the HyspIRI v1.0 and v2.0 band positions. This clearly shows an improvement in spectral contrast between the silicate spectra using v2.0 with the proposed shift of the 10.53 µm band shortward to 10.05 µm. An additional modification to the 10.05 µm band that could further increase spectral diversity between various silicate minerals and limit the amount of interference from the edge of the O_3 absorption region would be to narrow the response function itself. This modification is shown in Figure 19, including shifting of the 11.33 µm band to 11.35 µm for more accurate carbonate detection. Further simulations need to be performed in order to test the effects of narrowing the band response. These include possible issues with the sensitivity to O_3 absorption feature in this region, and possible degradation of the signal to noise of the detector response.

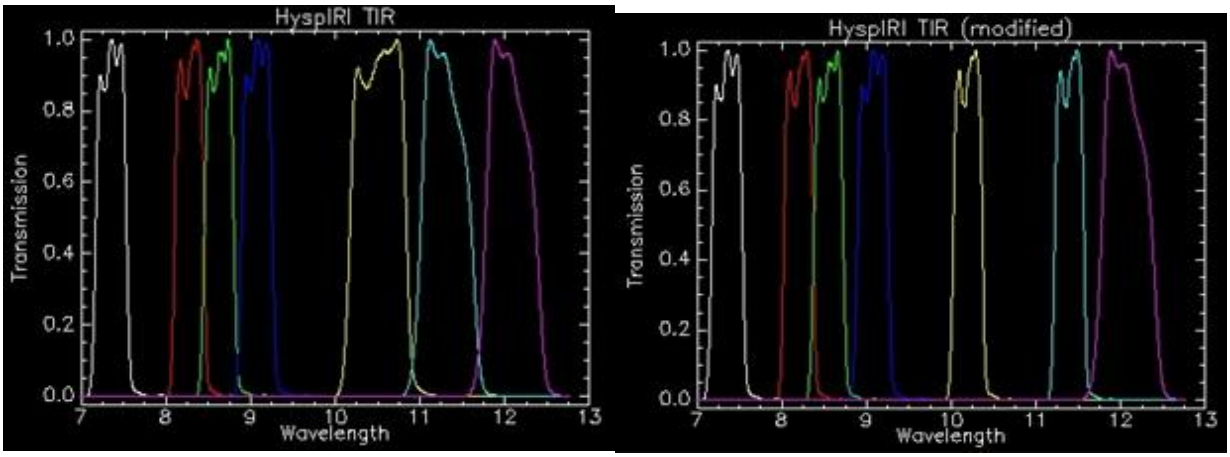

Figure 19. HyspIRI TIR response functions showing band positions for v1.0 (left) and the proposed v2.0 modifications including narrowing of the proposed 10.05 µm and 11.35 µm bands (right).

6.1.2 Case Study: Great Sands

The Gran Desierto dune system constitutes the largest portion of the Sonoran Desert in Mexico and the largest and most active sand sea in North America. *Scheidt et al.* [2011] showed that the central dune area consists of a mixture of approximately 90% quartz and 10% feldspar (plagioclase and potassium feldspar). The grain size, composition, texture, color and sorting have been well documented in previous studies [*Blount and Lancaster*, 1990; *Lancaster*, 1992]. Spatial variability in emissivity primarily occurs due to the distribution of quartz and feldspars across the central dune system via æolian deposits [*Scheidt et al.*, 2011].

Figure 20 shows linear deconvolution results for ASTER, HyspIRI v1.0 and v2.0 band positions for three sand samples collected over the Gran Desierto dune system in Mexico (SAM94, SAM39, SAMG162). The emissivity spectra of the three sand samples are shown top left, in addition to band positions that were modified in HyspIRI v2.0 (vertical red bars), and the unchanged HyspIRI v1.0 band positions (vertical gray bars). The three end members chosen for the Desierto samples included carbonate, feldspar, and quartz for SAM94, and feldspar and quartz for SAM39 and SAMG162, respectively. The table (top right) shows results of the spectral unmixing, and, assuming the lab results are regarded as 'truth', HyspIRI v2.0 matched the lab results more closely for SAM94 and SAM39 than HyspIRI v1.0, whereas the results for SAMG162 were similar.

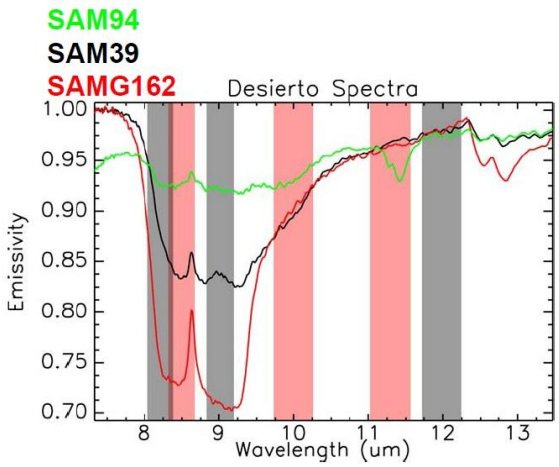

SAM94	LAB	ASTER	HYSP 1.0	HYSP 2.0
Carbonate	45.9	42.9	44.2	42.3
Feldspar	32.0	17.7	28.4	33.8
Quartz	22.1	39.4	27.3	23.9
RMS	0.0026	0.0017	0.0020	0.0022

SAM39	LAB	ASTER	HYSP 1.0	HYSP 2.0
Feldspar	64.1	74.0	72.4	65.9
Quartz	35.9	26.0	27.6	34.1
RMS	0.0038	0.0000	0.0011	0.0021

samG162	LAB	ASTER	HYSP 1.0	HYSP 2.0
Quartz	67.9	64.8	62.4	62.0
Feldspar	32.1	35.2	37.6	38.0
RMS	0.0026	0.0063	0.0037	0.0036

Figure 20. Linear deconvolution results for ASTER, HyspIRI v1.0 and v2.0 band positions for three sand samples collected over the Gran Desierto dune system in Mexico (SAM94, SAM39, SAMG162). Bottom image shows a view of the dune system, which contains primarily a mixture of quartz and feldspars.

Although the result for the carbonate end member were much the same for v1.0 and v2.0 for the SAM94 sample, it would still be useful to shift the current 11.33 µm band to a slightly higher position at 11.35 µm. This would allow more accurate resolution of a larger variety of different carbonate minerals. This is illustrated in Figure 21, which shows three different types of carbonate spectra from ASTlib including dolomite, calcite and siderite. Carbonates have a distinctive emissivity minimum in the 11–12 µm region. The gray bars show the modified v2.0 band positions, and it is clear that shifting the 11.33 µm band slightly to around 11.35–11.37 µm will better capture the response of all three different carbonate types in this region, especially dolomite.

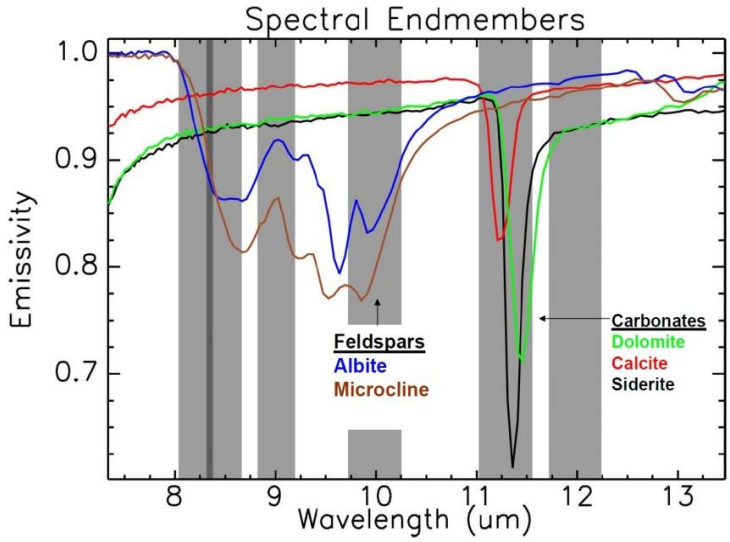

Figure 21. Laboratory spectra of feldspars, and carbonates, with HyspIRI v2.0 band positions shown as gray vertical bars.

6.1.3 Conclusions

Preliminary research studies on the optimum TIR band placement for Earth surface compositional mapping in support of the HyspIRI mission suggest a new HyspIRI TIR band configuration. The major modification involves moving the 10.53 µm band closer to 10 µm in order to better discriminate between quartz and feldspar minerals. This was demonstrated using linear deconvolution results with both laboratory and airborne remote sensing data. An additional modification to the 10.05 µm band that could further increase spectral diversity between various silicate minerals and limit the amount of interference from the edge of the O_3 absorption region would be to narrow the response function of the 10.05 µm band. Lastly, the 11.33 µm band should be shifted slightly to 11.35 µm in order to better encompass the absorption feature of different types of carbonates including dolomite, calcite and siderite in this region.

7 Future work with airborne data

7.1 HyTES

The Hyperspectral Thermal Emission Spectrometer (HyTES) is an airborne imaging spectrometer with 256 spectral channels between 7.5 and 12 micrometers in the thermal infrared part of the electromagnetic spectrum and 512 pixels cross-track with pixel sizes in the range 5-50 m depending on aircraft altitude [*Johnson et al.*, 2011]. HyTES is being developed to support the HyspIRI mission and will provide precursor data at much higher spatial and spectral resolutions to help determine the optimum band positions for the HyspIRI-TIR instrument as well as provide precursor datasets for Earth Science research. HyTES completed its first flights during July 2012 and incorporates several new technologies including a Dyson spectrometer, long, straight slit, curved diffraction grating and Quantum Well Infrared Photodetector (QWIP) [*Johnson et al.*, 2009]. The model for the HyTES instrument is shown in Fig. 22.

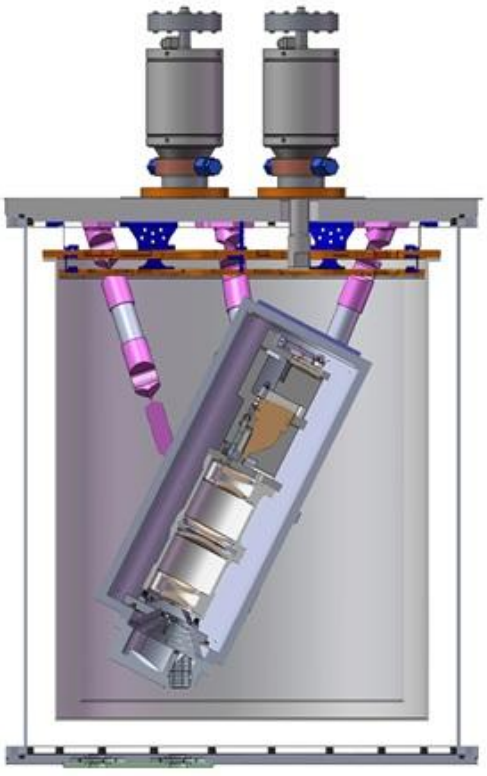

Instrument Characteristic	HyTES
Mass (Scanhead)[1]	12kg
Power	400W
Volume	1m x 0.5m (Cylinder)
Number of pixels x track	512
Number of bands	256
Spectral Range	7.5-12 µm
Frame speed	35 or 22 fps
Integration time (1 scanline)	28 or 45 ms
Total Field of View	50 degrees
Calibration (preflight)	Full aperture blackbody
Detector Temperature	40K
Spectrometer Temperature	100K
Slit Length and Width	20 mm x 39 µm
IFOV	1.7066
Pixel Size/Swath at 2000 m flight altitude[2]	3.41m/1868.33m
Pixel Size/Swath at 20,000 m flight altitude[2]	34.13m/18683.31m

Figure 22. (left) The model for the HyTES instrument, including a Dyson spectrometer, long, straight slit, curved diffraction grating and Quantum Well Infrared Photodetector (QWIP). (right) HyTES instrument specifications.

Table 2. Test sites and purpose for the HyTES test flights.

Sitename	Purpose
La Brea Tarpits	Urban/Methane
Salton Sea	Calibration/Ammonia
Huntington Gardens	Ecosystems
Cuprite	Surface Composition
Death Valley	Surface Composition
Navajo Generating Station	Sulfur dioxide

Table 2 shows the test sites that HyTES flew over during July 2012 and their purpose, while Fig. 23 shows the site locations on a Google Earth image. The purpose of the different sites range from trace gas detection (e.g. methane, ammonia, sulfur dioxide), to calibration and surface composition mapping.

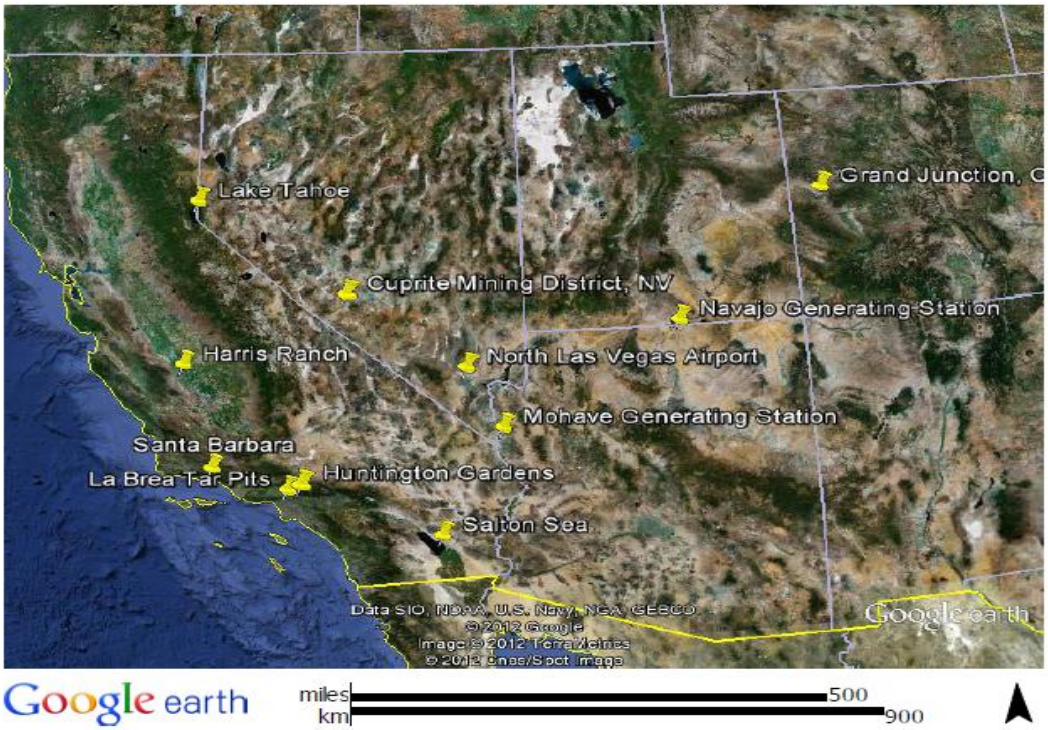

Figure 23. Test site locations on Google Earth.

An example of HyTES image acquired on 07-20-2012 over Cuprite, NV with bands 150 (10.08 µm), 100 (9.17 µm), and 58 (8.41 µm) displayed as RGB respectively and as image cube is shown in Fig. 24. Fig. 24 A shows the radiance at sensor for different locations at Cuprite, NV. Atmospheric features can be seen primarily in the 7.5-8.5 µm and >11.5µm regions and are mostly due to water vapor absorption. Fig. 24 B shows the Noise Equivalent Delta Temperature (NEDT) histogram distribution was ~0.2 K for this image.

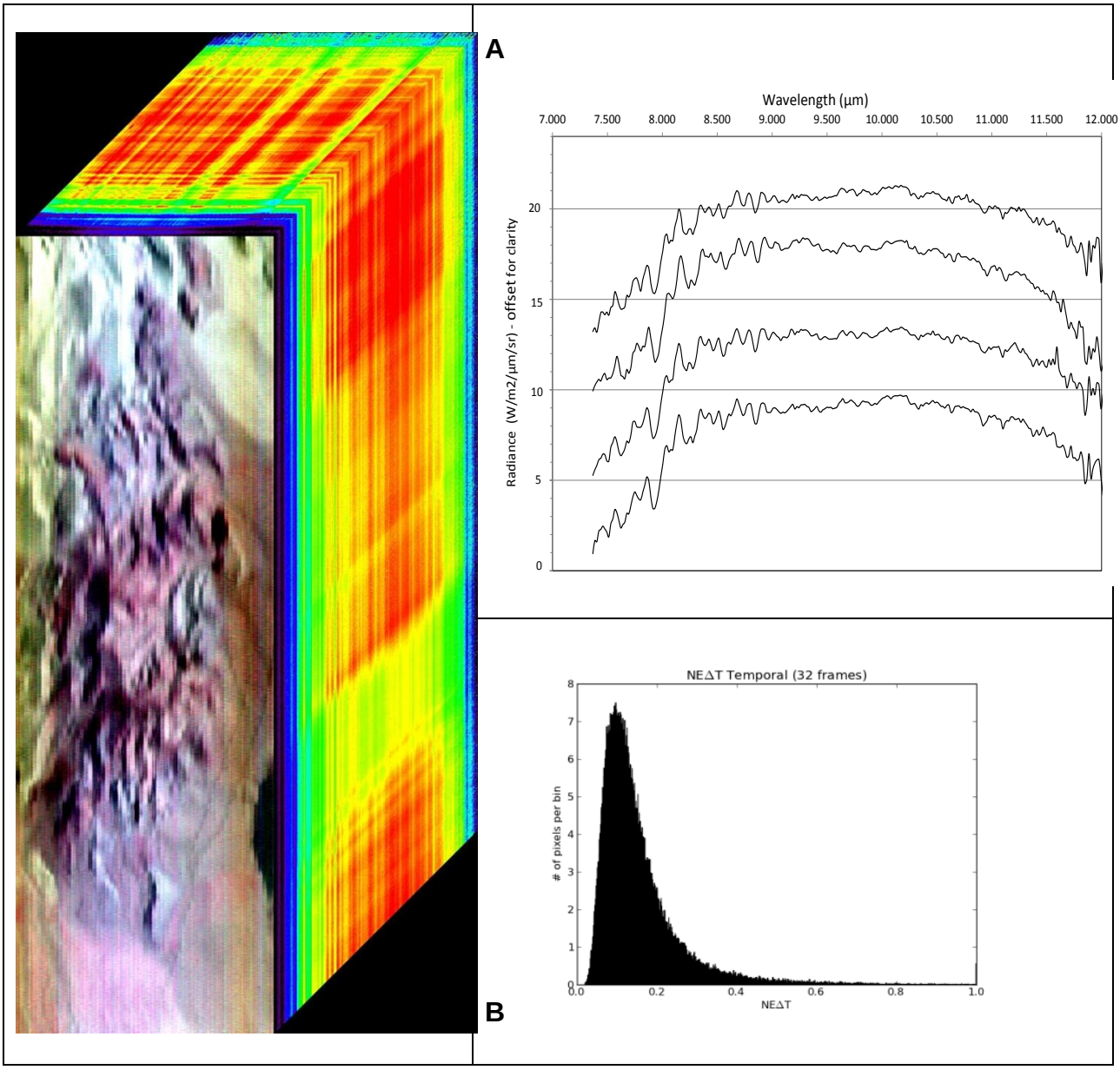

Figure 24. (left) Cuprite, NV image acquired on 07-20-2012 with bands 150 (10.08 µm), 100 (9.17 µm), and 58 (8.41 µm) displayed as RGB respectively as image cube. A) Radiance at sensor for different locations at Cuprite, B) Noise equivalent Delta Temperature (NEDT) histogram (~0.2 K).

Fig. 25 shows comparison between HyTES emissivity spectra and laboratory spectra of geologic samples collected over the Cuprite, NV site. The HyTES spectra were convolved to the nominal HyspIRI v1.0 band positions (blue circles) as well as the lab data (red circles) for comparison. The HyTES emissivity spectra were retrieved using the ASTER Temperature Emissivity Separation (TES) algorithm, and the calibration curve was modified for HyspIRI bands using a set of ~150 lab spectra consisting of rocks, sands, soils, vegetation, ice, water, and snow. Atmospheric correction was accomplished using MODTRAN 5.2 radiative transfer code with input atmospheric profiles of air temperature, relative humidity, and geopotential height from the NCEP-GDAS product. The spectra show comparisons at four sites with a variety of lithologies including areas of carbonate (Ca),

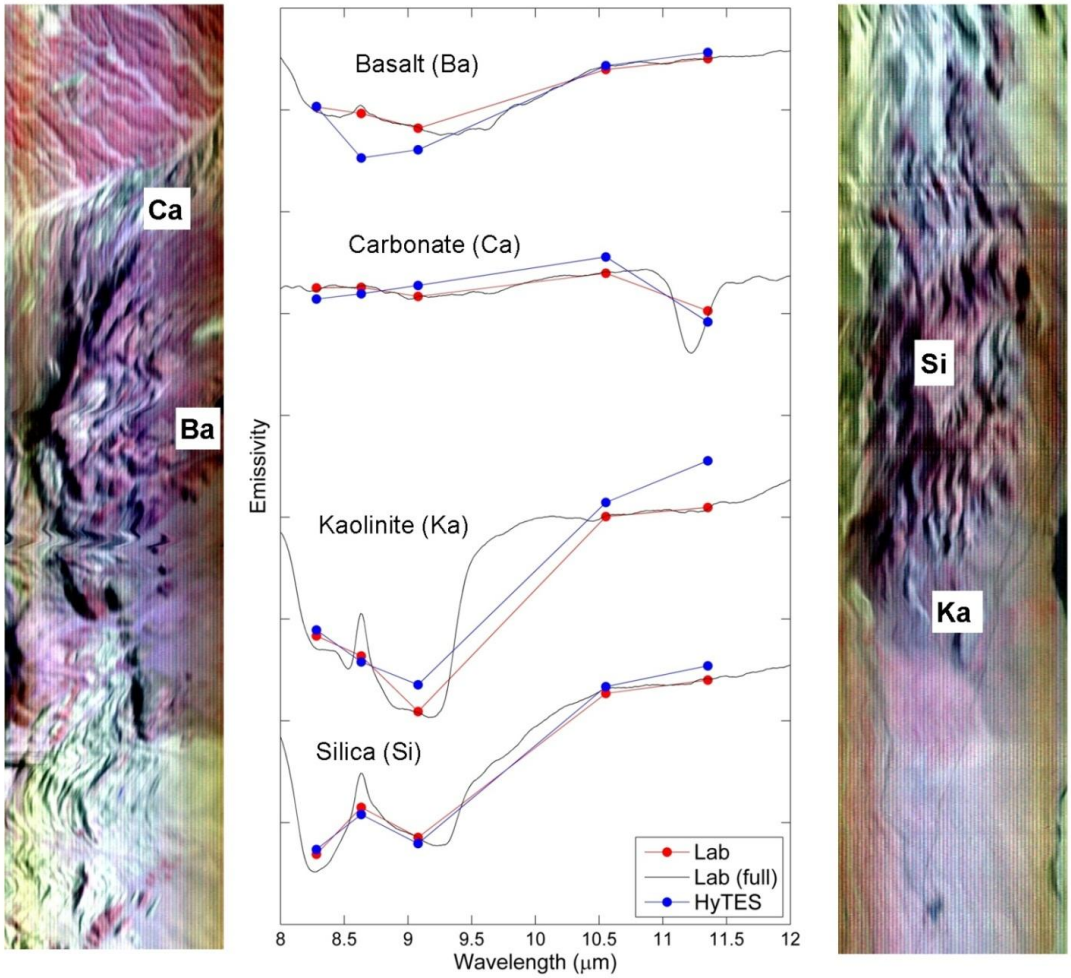

Figure 25. Comparisons between HyTES spectra convolved to HyspIRI TIR bands (blue circles) and laboratory spectra (red circles) of geologic samples collected in the Cuprite, NV region including basalt, carbonate, kaolinite, and silica.

basalt (Ba), kaolinite (Ka), and silica (Si). The lab spectra were obtained by measuring the reflectance of weathered surfaces of the field samples with the Jet Propulsion Laboratory Fourier Transform Infrared Spectrometer (JPL-FTIR). The reflectance measurements were converted to emissivity using Kirchoff's law, and then resampled to the HyspIRI response functions.

The laboratory spectra from the area of kaolinite have a strong broad emission minima across HyspIRI bands 8.3, 8.6, and 9.1 μm. This feature is typical of these clay minerals. The spectrum from the area of silica has two emission minima located in HyspIRI 8.3 and 9.1 μm bands. These are typical of fairly pure samples of quartz and result from Si-0 stretching. In general, the shape of the image spectra retrieved from HyTES agrees well with the laboratory spectra. This gives confidence that band studies involving HyTES data will be possible in future work. Different band combinations and response shapes will be tested using the high spectral resolution data to assess the most optimal band positions for SO_2 mapping and associated atmospheric correction, as well as mineral mapping.

7.2 MAGI

The Mineral and Gas Identifier (MAGI) was recently developed and flown by The Aerospace Corporation with funding under the NASA Instrument Incubator Program (IIP). The airborne instrument has 32 channels in the thermal infrared (TIR) region spanning from 7.1 – 12.7 micrometers (Table 1). It consists of a whiskbroom design that can acquire up to 2800 pixels in the cross track direction by 128 pixels on the downtrack direction [*Hall et al.*, 2008]. Each of these scans constitute one "whisk" and the number of whisks is a function of the desired scan line length. This approach allows for wide crosstrack scanning over multiple channels, which is a significant improvement over previous hyperspectral TIR scanners such as the Spatially Enhanced Broadband Array Spectrograph System (SEBASS) sensor [*Hackwell et al.*, 1996]. For example, SEBASS is a pushbroom design and only acquires 128 pixels in the crosstrack direction resulting in limited areal coverage at the typical 1m/pixel spatial resolution.

Table 3. MAGI instrument specifications.

Number of spectral channels	32
Wavelength coverage	7.1 – 12.7 µm
Instantaneous pixel FOV	0.53 mrad
Frame rate	955 Hz
Integration Time	280 µsec
NEDT (single frame)	~0.12°C at 10 µm
Number of along-track pixels	128
Maximum cross-track scan angle	± 42° (2800 pixels)
Max. number of cross-track scans	unlimited
Detector	HgCdTe
Detector Temperature	55 K
Optics Temperature	120 K
Calibration	Full aperture BB

MAGI was developed to test new TIR technologies and systems for future spaceborne TIR sensors such as HyspIRI. The sensor relies on a novel optical design that incorporates a Dyson spectrometer that has small optical distortion at low f-numbers. This spectrometer is mated to a HgCdTe focal plane array, which allows high frame rate data with very high signal to noise. Cryocoolers are used to cool the focal plane and optical bench, and an external telescope assembly sets the desired pixel IFOV (Figure 26).

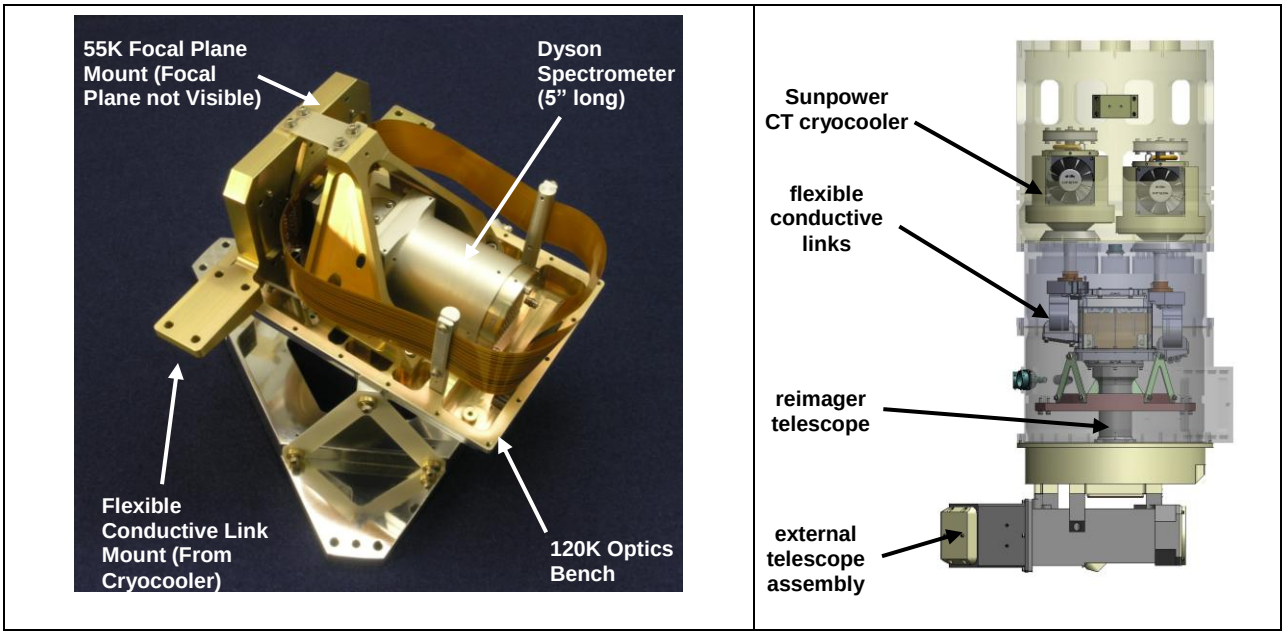

Figure 26. (left) Heart of the MAGI sensor showing Dyson spectrometer, mounts, and optics bench. (right) Sensor dewar with external telescope (dewar diameter is 13 inches).

The number of instrument channels was selected specifically to optimize the data return, span the entire wavelength region with no gaps, minimize spectral redundancy, and increase the signal to noise. Prior to building MAGI, trade studies were conducted using laboratory and SEBASS hyperspectral data to determine the optimal number of bands needed to discriminate most geologic and urban materials as well as common natural and anthropogenic gases. For both gas detection and mineral mapping studies, the spectral resolution of these hyperspectral datasets was iteratively degraded by factors of two to assess the point at which serious loss of detection fidelity sets in. The starting resolution was represented by the SEBASS configuration of 128 spectral channels spanning 7.65 to 13.55 μm. Degradations were then made to 64, 32, and 16 spectral channels across this same spectral range. Appropriate degradations were also made on the target end-member spectra chosen for the surface-mapping study and target gas spectra used for the gas detection study (Figure 27).

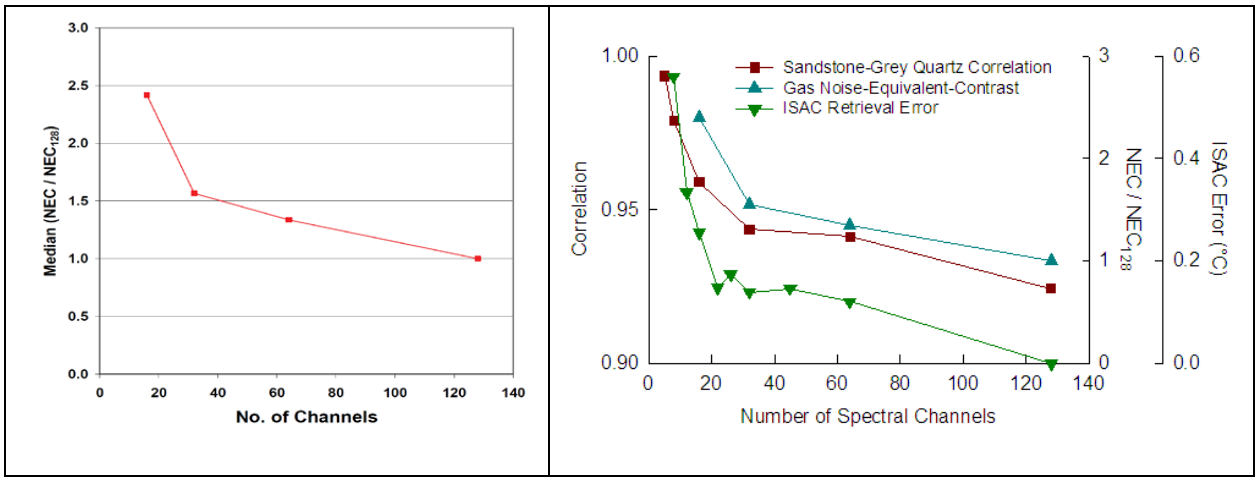

Figure 27. (left) Noise Equivalent Contrast (NEC) median ratio vs. number of channels (128, 64, 32, and 16) for 28 chemical compounds common in industrial gas plumes [*Hall et al.,* 2008]. Larger ratios suggest a lower sensitivity to the specific chemical. In most cases sensitivity loss from 128 channels to 32 is less than a factor of 2. However, note the significant penalty where the data is reduced to less than ~ 30 channels. (right) Similar plot for other materials and gases as well as the surface temperature retrieval error expected the in-scene atmospheric correction (ISAC).

The initial flights of MAGI were conducted in December 2011 and include geologic targets such as the Salton Sea and Coso geothermal fields in CA and Cuprite in NV; agricultural targets such as portions of the Central Valley in CA; as well as urban targets in Los Angeles and El Segundo in CA. Atmospherically-corrected data from one whisk of the Salton Sea flight line is presented in Figure 28 and shows the excellent spatial and spectral quality of the data.

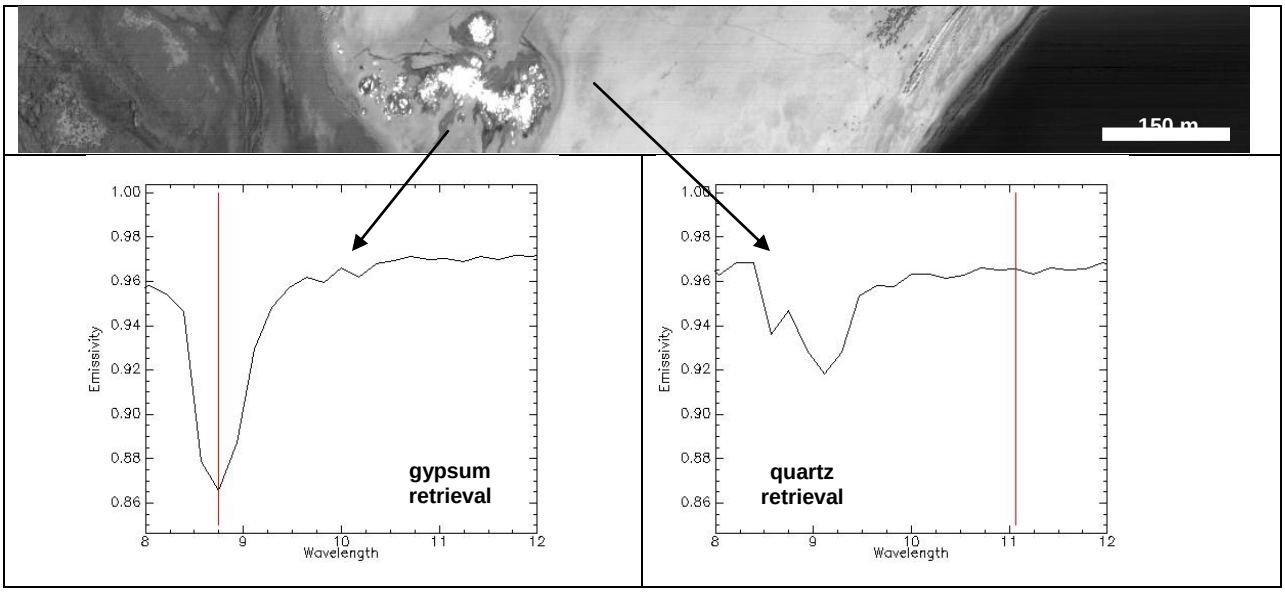

Figure 28. MAGI level 2 atmospherically-corrected data (whisk 18) and emissivity spectral retrievals from the Salton Sea, CA. (top) MAGI band 10 (8.751 micrometers) showing the "sandbar" geothermal field in the center of the strip and the Salton Sea to the right (north is to the upper right in the image). (left) Gypsum emissivity spectrum. (right) Quartz emissivity spectrum.

In order to test the accuracy of surface mineral retrievals using the currently-proposed HyspIRI TIR bandpasses, both MAGI TIR and the higher spectral resolution SEBASS TIR data were resampled to the six HyspIRI channels in the 8 – 12 micrometer region. The data were also resampled using the slightly altered band positions shown in Figure 19, which includes a narrower bandwidth at 10.05 micrometers. The resampled data were then subjected to linear spectral deconvolution using a library of common minerals known to occur in the region, including (but not limited to) quartz, gypsum, calcite, anhydrite, halite, oligoclase, microcline, and montmorillonite (a clay mineral). Of particular interest in this case study was the ability to detect the feldspar minerals (e.g., oligoclase and microcline) and carbonate minerals (e.g., calcite) in each bandpass configuration. Figure 29 shows the results for one of the mineral identification tests.

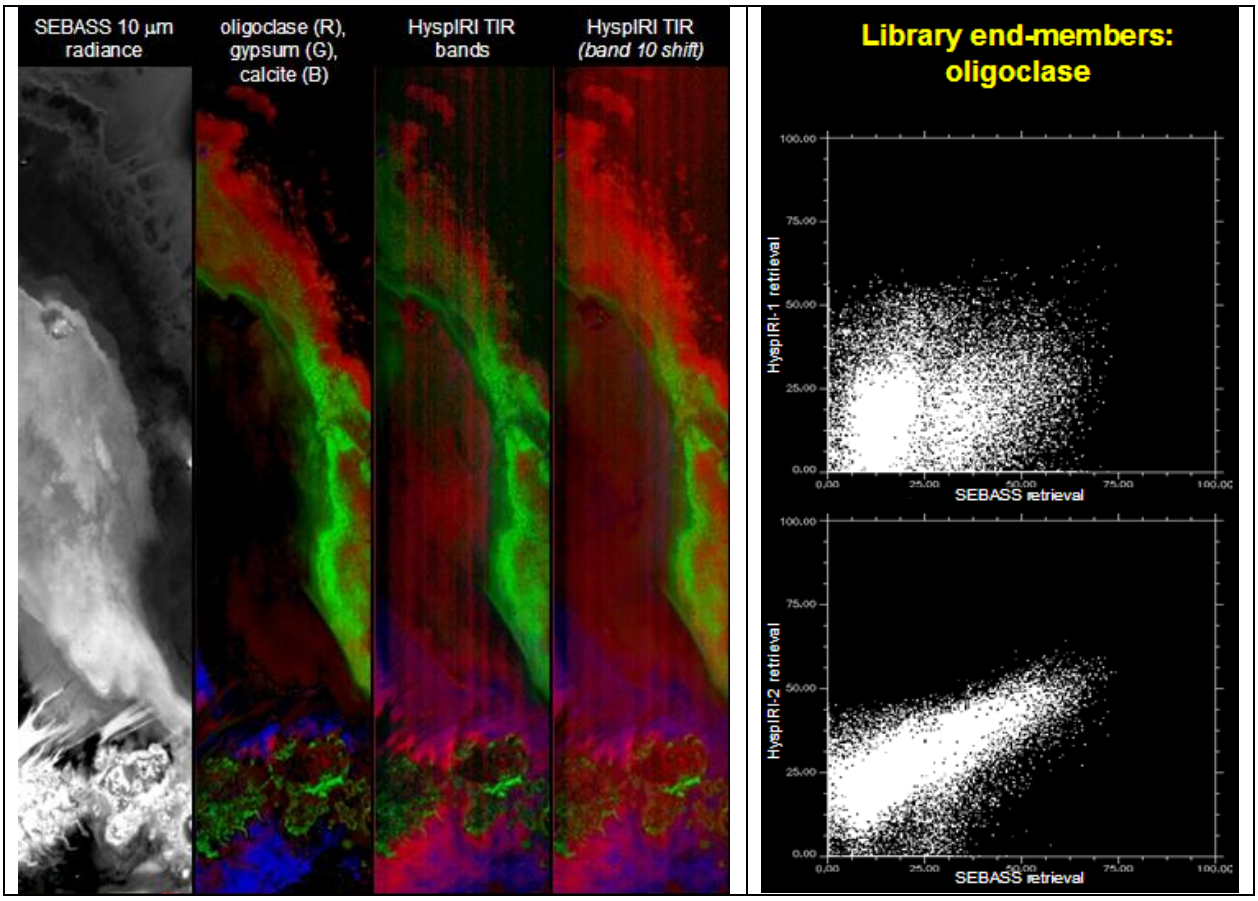

Figure 29. (left) Four panel image showing SEBASS data acquired over the "sandbar" geothermal field at Salton Sea, CA on April 6, 2010. The mineral retrieval for the full spectral resolution of SEBASS (second panel) is compared to both HyspIRI TIR configurations. The fourth panel shows an oligoclase distribution (in red) more similar to the full spectral resolution. (right) Scatter plots of the oligoclase retrievals confirm that there is a more linear relationship between the full spectral resolution and the simulated HyspIRI TIR data with the shifted band centers.

The initial results of the band position study using SEBASS and MAGI data both confirm that movement (and narrowing) of the 10 micron channel will greatly improve our ability to detect feldspar minerals and distinguish this class of minerals from other silicates. This will be important for surface change detection and mapping using a future HyspIRI TIR sensor. Furthermore, the proposed band shifts do not significantly change the ability to detect other minerals (e.g., quartz and calcite), which do not have emissivity features in the regions affected by the band position changes. Future work will be carried out using MAGI and SEBASS to assess the proposed position changes on other surface and gas detections.

8 References

Baldridge, A. M., S. J. Hook, C. I. Grove, and G. Rivera (2009), The ASTER Spectral Library Version 2.0, *Remote Sensing of Environment*, *114*(4), 711-715.

Berk, A., et al. (2005), MODTRAN^{TM} 5, A Reformulated Atmospheric Band Model with Auxiliary Species and Practical Multiple Scattering Options: Update, in *Algorithms and Technologies for Multispectral, Hyperspectral, and Ultraspectral Imagery XI*, edited by S. S. Sylvia and P. E. Lewis, Proceedings of SPIE, Bellingham, WA.

Blount, G., and N. Lancaster (1990), Development of the Gran Desierto Sand Sea, Northwestern Mexico, *Geology*, *18*(8), 724-728.

Duda, K. A., M. Ramsey, R. Wessels, and J. Dehn (2009), Optical satellite volcano monitoring: A multi-sensor rapid response system, in: P.P. Ho, (ed.), Geoscience and Remote Sensing, *INTECH Press, Vukovar, Croatia, ISBN 978-953-307-003-2*, 473-496.

Campion, R., G.G. Salerno, P-F. Coheur, D. Hurtmans, L. Clarisse, K. Kazahaya, M. Burton, T. Caltabiano, C. Clerbaux, and A. Bernard (2010), Measuring volcanic degassing of SO2 in the lower troposphere with ASTER band ratios, *J. Volcanol. Geotherm. Res.*, *194*, 42-54.

Corradini, S., L. Merucci, A. J. Prata, and A. Piscini (2010), Volcanic ash and SO_2 in the 2008 Kasatochi eruption: Retrievals comparison from different IR satellite sensors, *J. Geophys. Res.*, *115*, D00L21, doi:10.1029/2009JD013634.

Edgett, K. S., and N. Lancaster (1993), Volcanoclastic aeolian dunes: terrestrial examples and applications to martian sands, *Journal of Arid Environments*, *25*, 271-297.

Hackwell, J. A., D. W. Warren, R. P. Bongiovi, S. J. Hansel, T. L. Hayhurst, D. J. Mabry, M. G. Sivjee, and J. W. Skinner (1996), LWIR/MWIR imaging hyperspectral sensor for airborne and ground-based remote sensing, *in SPIE Imaging Spectrometry II, vol. 2819, M.R. Descour and J.M. Mooney, Eds.*, pp. 102-107.

Hall, J. L., J. A. Hackwell, D. M. Tratt, D. W. Warren, and S. J. Young (2008), Space-based mineral and gas identification using a high-performance thermal infrared imaging spectrometer, *Proceedings of SPIE 7082, 70820M. http://dx.doi.org/10.1117/12.799659.*

Hook, S. J., E. A. Abbott, C. Grove, A. B. Kahle, and F. D. Palluconi (1999), Use of multispectral thermal infrared data in geologic studies, *Remote Sensing for the Earth Sciences:*

Manual of remote sensing, vol. 3 (E.N. Rencz ed.), (3rd ed.) (pp. 59-110). New York: John Wiley and Sons.

Hook, S. J., J. E. J. Myers, K. J. Thome, M. Fitzgerald, and A. B. Kahle (2001), The MODIS/ASTER airborne simulator (MASTER) - a new instrument for earth science studies, *Remote Sensing of Environment*, *76*(1), 93-102.

Hook, S. J., J. E. Dmochowski, K. A. Howard, L. C. Rowan, K. E. Karlstrom, and J. M. Stock (2005), Mapping variations in weight percent silica measured from multispectral thermal infrared imagery - Examples from the Hiller Mountains, Nevada, USA and Tres Virgenes-La Reforma, Baja California Sur, Mexico, *Remote Sensing of Environment*, *95*(3), 273-289.

Hunt, G. R. (1980), Electromagnetic radiation: the communication link in remote sensing, *Remote Sensing in Geology (B. S. Siegal and A.R. Gillespie, Eds.)*, Wiley, New York, pp. 5-45.

HyspIRI (2008), NASA 2008 HyspIRI Whitepaper and Workshop Report, *Jet Propulsion Laboratory, California Institute of Technology, Pasadena, California*, May 2009.

Johnson, W. R., S. J. Hook, P. Mouroulis, D. W. Wilson, S. D. Gunapala, C. J. Hill, J. M. Mumolo, and B. T. Eng (2009), Quantum well earth science testbed, *Infrared Physics & Technology*, *52*(6), 430-433.

Johnson, W. R., S. J. Hook, P. Mouroulis, D. W. Wilson, S. D. Gunapala, V. Realmuto, A. Lamborn, C. Paine, J. M. Mumolo, and B. T. Eng (2011), HyTES: Thermal imaging spectrometer development, AERO '11 Proceedings of the 2011 IEEE Aerospace Conference, pp 2011-2018, Washington DC, USA, 2011.

Justice, C. O., et al. (1998), The Moderate Resolution Imaging Spectroradiometer (MODIS): Land remote sensing for global change research, *IEEE Transactions on Geoscience and Remote Sensing*, *36*(4), 1228-1249.

Kearney, C.S., K. Dean, V.J. Realmuto, I.M. Watson, J. Dehn, and F. Prata (2008), Observations of SO2 production and transport from Bezymianny volcano, Kamchatka using the MODerate resolution Infrared Spectroradiometer (MODIS), *Int. J. Remote Sens.*, *29(22)*, 6647–6665.

Kearney, C., I. M. Watson, G. J. S. Bluth, S. Carn, and V.J. Realmuto (2009), A comparison of thermal infrared and ultraviolet retrievals of SO2 in the cloud produced by the 2003 Al-Mishraq State sulfur plant fire, *Geophys. Res. Lett., 36, L10807*, doi:10.1029/ 2009GL038215.

Kneizys, F. X., et al. (1996), The MODTRAN 2/3 Report & LOWTRAN 7 Model, F19628-91-C-0132, in *Phillips Lab*, edited, Hanscom AFB, MA.

Lancaster, N. (1992), Relations between Dune Generations in the Gran Desierto of Mexico, *Sedimentology*, *39*(4), 631-644.

Prata, A. J., G. Bluth, B. Rose, D. Schneider, and A. Tupper (2001), Failures in detecting volcanic ash from a satellite-based technique - Comments, *Remote Sensing of Environment*, *78*(3), 341-346.

Prata, A. J., D. M. O'Brien, W.I. Rose, and S. Self (2003), Global, long-term sulphur dioxide measurements from TOVS data: a new tool for studying explosive volcanism and climate, *Geophysical Monograph 139*, 75 - 92.

Prata, A. J., and C. Bernardo (2007), Retrieval of volcanic SO_2 column abundance from Atmospheric Infrared Sounder data, *J. Geophys. Res.*, *112*, D20204, doi:10.1029/2006JD007955

Pugnaghi, S., G. Gangale, S. Corradini, M.F. Buongiorno (2006), Mt. Etna sulfur dioxide flux monitoring using ASTER-TIR data and atmospheric observations, *J. Volcanol. Geotherm. Res.*, *152*, 74-90.

Ramsey, M., and S. Rose (2009), The complex effects of subpixel compositional, thermal and textural heterogeneities on spaceborne TIR data, in *The 2009 HyspIRI Science Workshop*, edited, Pasadena, CA.

Ramsey, M. S., and P. R. Christensen (1998), Mineral abundance determination: Quantitative deconvolution of thermal emission spectra, *Journal of Geophysical Research-Solid Earth*, *103*(B1), 577-596.

Ramsey, M. S., P. R. Christensen, N. Lancaster, and D. A. Howard (1999), Identification of sand sources and transport pathways at the Kelso Dunes, California, using thermal infrared remote sensing, *Geological Society of America Bulletin*, *111*(5), 646-662.

Ramsey. M. S., and A. J. L. Harris (2012), Volcanology 2020: How will thermal remote sensing of volcanic surface activity evolve over the next decade?, *J. Volcanol. Geotherm. Res.*, *10.1016/j.jvolgeores.2012.05.011*.

Realmuto, V. J., and H. M. Worden (2000), Impact of atmospheric water vapor on the thermal infrared remote sensing of volcanic sulfur dioxide emissions: A case study from the Pu'u 'O'o vent of Kilauea Volcano, Hawaii, *Journal of Geophysical Research-Solid Earth*, *105*(B9), 21497-21507.

Realmuto, V. J., A. J. Sutton, and T. Elias (1997), Multispectral thermal infrared mapping of sulfur dioxide plumes: A case study from the East Rift Zone of Kilauea Volcano, Hawaii, *Journal of Geophysical Research-Solid Earth*, *102*(B7), 15057-15072.

Realmuto, V. J., M. J. Abrams, M. F. Buongiorno, and D. C. Pieri (1994), The Use of Multispectral Thermal Infrared Image Data to Estimate the Sulfur-Dioxide Flux from Volcanos - a Case-Study from Mount Etna, Sicily, July 29, 1986, *Journal of Geophysical Research-Solid Earth*, *99*(B1), 481-488.

Realmuto, V, S. Hook, M. Foote, I. Csiszar, P. Dennison, L. Giglio, M. Ramsey, R.G. Vaughan, M. Wooster, R. Wright (2011), HyspIRI High-Temperature Saturation Study, Jet Propulsion Laboratory, California Institute of Technology, Publication 11-2, April 2011, http://hyspiri.jpl.nasa.gov/downloads/2011_High_Temperature_Saturation_Report/HyspIRI_High-Temperature_Saturation_Report_110519.pdf

Rose, W.I., Y. Gu, I. M. Watson1, T. Yu1, G. J. S. Bluth1, A. J. Prata, A. J. Krueger, N. Krotkov, S. Carn, M. D. Fromm, D. E. Hunton, G. G. J. Ernst, A. A. Viggiano, T. M. Miller, J. O. Ballenthin, J. M. Reeves, J. C. Wilson, B. E. Anderson, and D. E. Flittner (2003), The February–March 2000 Eruption of Hekla, Iceland from a Satellite Perspective, *Geophysical Monograph 139*, 107-132.

Rosi, M., A. Bertagnini, A. J. L. Harris, L. Pioli, M. Pistolesi, and M., Ripepe (2006), A case history of paroxysmal explosion at Stromboli: timing and dynamics of the April 5, 2003 event. *Earth and Planetary Science Letters 243*, 594–606.

Rybin, A., M. Chibisova, P. Webley, T. Steensen, P. Izbekov, C. Neal, and V. Realmuto (2011), Satellite and ground observations of the June 2009 eruption of Sarychev Peak volcano, Matua Island, Central Kuriles, *Bull. Volcanol.*, doi: 10.1007/s00445-011-0481-0

Scheidt, S., N. Lancaster, and M. Ramsey (2011), Eolian dynamics and sediment mixing in the Gran Desierto, Mexico, determined from thermal infrared spectroscopy and remote-sensing data, *Geological Society of America Bulletin*, *123*(7-8), 1628-1644.

Teggi, S., M.P Bogliolo, M.F. Buongiorno, S. Pugnaghi, and A. Sterni (1999), Evaluation of SO2 emission from Mount Etna using diurnal and nocturnal multispectral IR and visible imaging spectrometer thermal IR remote sensing images and radiative transfer models, *J. Geophys. Res.*, *104(B9)*, 20,069-20,079.

Thomas, H.E., I.M. Watson, C. Kearney, S.A. Carn, and S.J. Murray (2009), A multi-sensor comparison of sulphur dioxide emissions from the 2005 eruption of Sierra Negra volcano, Galápagos Islands, Remote Sens. Environ., 113, 1331–1342.

Tupper, A., J. Davey, P. Stewart, B. Stunder, R. Servranckx, and F. Prata (2006), Aircraft encounters with volcanic clouds over Micronesia, Oceania, 2002-03, *Aust Meteorol Mag*, *55*(4), 289-299.

Urai, M. (2004), Sulfur dioxide flux estimation from volcanoes using Advanced Spaceborne Thermal Emission and Reflection Radiometer – a case study of Miyakejima volcano, Japan, *J. Volcanol. Geotherm. Res.*, *134*, 1-13.

Vaughan, R. G., S. J. Hook, W. M. Calvin, and J. V. Taranik (2005), Surface mineral mapping at Steamboat Springs, Nevada, USA, with multi-wavelength thermal infrared images, *Remote Sensing of Environment*, *99*(1-2), 140-158.

Watson, I. M., V. J. Realmuto, W. I. Rose, A. J. Prata, G. J. S. Bluth, Y. Gu, C. E. Bader, and T. Yu (2004), Thermal infrared remote sensing of volcanic emissions using the moderate resolution imaging spectroradiometer, *Journal of Volcanology and Geothermal Research*, *135*(1-2), 75-89.

Wolfe, R. E., D. P. Roy, and E. Vermote (1998), MODIS land data storage, gridding, and compositing methodology: Level 2 grid, *IEEE Transactions on Geoscience and Remote Sensing*, *36*(4), 1324-1338.

Yamaguchi, Y., A. B. Kahle, H. Tsu, T. Kawakami, and M. Pniel (1998), Overview of Advanced Spaceborne Thermal Emission and Reflection Radiometer (ASTER), *IEEE Transactions on Geoscience and Remote Sensing*, *36*(4), 1062-1071.